Shrunken Locally Linear Embedding for Passive Microwave Retrieval of Precipitation

Ardeshir M. Ebtehaj, Rafael L. Bras, and Efi Foufoula-Georgiou

***Abstract*—This paper introduces a new Bayesian approach to the inverse problem of passive microwave rainfall retrieval. The proposed methodology [called the shrunken locally linear embedding algorithm for retrieval of precipitation (ShARP)] relies on a regularization technique and makes use of two joint dictionaries of coincident rainfall profiles and their corresponding upwelling spectral radiative fluxes. A sequential detection–estimation strategy is adopted, which basically assumes that similar rainfall intensity values and their spectral radiances live close to some sufficiently smooth manifolds with analogous local geometry. The detection step employs a nearest neighbor classification rule, whereas the estimation scheme is equipped with a constrained shrinkage estimator to ensure the stability of retrieval and some physical consistency. The algorithm is examined using coincident observations of the active precipitation radar and the passive microwave imager onboard the TRMM satellite. We present promising results of instantaneous rainfall retrieval for some tropical storms and mesoscale convective systems over ocean, land, and coastal zones. We provide evidence that the algorithm is capable of properly capturing different storm morphologies including high-intensity rain cells and trailing light rainfall, particularly over land and coastal areas. The algorithm is also validated at an annual scale for calendar year 2013 versus the standard (version 7) radar (2A25) and radiometer (2A12) rainfall products of the TRMM satellite.**

***Index Terms*—Data processing, inverse problem, radar, radiometry, rainfall passive retrieval, regularization.**

I. Introduction

In THE mathematical sense, rainfall retrieval from remotely sensed observations is an inverse problem in which we aim to estimate the rainfall intensity from its indirect and noisy measurements. The passive retrieval of rainfall from upwelling spectral radiances is one of the most challenging atmospheric retrieval problems chiefly because rainfall spectral signatures are often undersampled, significantly corrupted with the background radiation, and are nonlinearly related to the rainfall vertical profile. The retrieval of rainfall from visible and infrared observations typically relies on empirical approaches as the measurements only respond to the radiative fluxes from the upper portion of the cloud layers (e.g., see [1]–[8]). In microwave wavelengths ($\sim$6–200 GHz), the hydrometeor vertical profile alters the upwelling radiation in the entire atmospheric column through absorption–emission and scattering processes. Over ocean, the absorption–emission of the atmospheric liquid water can be well distinguished from the cold background by the physical laws of radiative transfer [9], [10]. In addition, the attenuation of the polarized ocean surface emission by atmospheric hydrometeors (see [11]–[14] and the references therein) and scattering by ice particles [10], [15] give rise to a high signal-to-noise ratio in the rainfall spectral signatures, making the retrieval problem more straightforward over ocean than over land. Over land, the radiation from highly emissive heterogeneous land surfaces often masks the hydrometeor emission signal, forcing the retrieval approaches to mostly rely on the complex scattering effects of the ice particles in the raining clouds [16]–[18]. As a result of these major differences over ocean and land, two classes of physically based and empirical microwave retrieval algorithms have emerged. The empirical approaches have been predominantly used for retrieval over land, whereas the physically based methods have been used over ocean.

Over ocean, the physically based methods typically follow two distinct strategies. The first family of these algorithms [9] simplifies the basic radiative transfer equation for atmospheric constituents under axially symmetric scattering and the Rayleigh–Jeans approximation. Given the observed spectral radiative fluxes with minimal scattering effect, the simplified equations make it possible to obtain atmospheric absorptivity, the drop-size distribution, and, thus, the rainfall intensity profile. The second class of methodologies (e.g., see [12] and [19]–[25]), which is known as the Bayesian retrieval approaches, exploits a statistically representative *a priori* generated database that encodes the correspondence between spectral brightness temperatures and rainfall profiles. In physically generated databases, the causal relationships between the precipitation profiles and their upwelling spectral radiances are modeled using a combination of cloud resolving and radiative transfer models. Sophisticated numerical cloud resolving models (e.g., the Goddard Cumulus Ensemble model) are used to produce a large collection of raining and nonraining cloud structures with distinct hydrometeor profiles. Then, for all of these profiles, a

Manuscript received August 14, 2014; revised November 4, 2014; accepted December 10, 2014. This work was supported in part by a NASA Earth and Space Science Fellowship under Contract NNX12AN45H, by the K. Harrison Brown Family Chair, by the Ling Endowed Chair Funding, by two NASA Global Precipitation Measurement Grants under Contract NNX13AH35G and Contract NNX13AG33G, and by the Belmont Forum DELTAS Grant under Contract ICER-1342944.

A. M. Ebtehaj is with the School of Civil and Environmental Engineering, College of Engineering, Georgia Institute of Technology, Atlanta, GA 30332 USA (e-mail: mebtehaj@gatech.edu).

R. L. Bras is with the School of Civil and Environmental Engineering, College of Engineering and the School of Earth and Atmospheric Sciences, College of Sciences, Georgia Institute of Technology, Atlanta, GA 30332 USA (e-mail: rlbras@gatech.edu).

E. Foufoula-Georgiou is with the Department of Civil, Environmental, and Geo-Engineering, College of Science and Engineering, University of Minnesota, Minneapolis, MN 55414 USA (e-mail: efi@umn.edu).

Digital Object Identifier 10.1109/TGRS.2014.2382436

radiative transfer model is employed to obtain their spectral radiances at the top of the atmosphere. Finally, this database is utilized to retrieve rainfall profiles from observed microwave radiances using an inversion scheme. This approach has been the cornerstone of the Goddard Profiling Algorithm (GPROF) [23]–[25] used to produce the TRMM operational passive retrieval products. On the other hand, over land, empirical methods typically rely on a scattering index [26], [27], which relates the depression in the high-frequency channels (e.g., 85 GHz) to the surface rainfall, in response to the frozen hydrometeors commonly found in the raining clouds. The magnitude of the high-frequency depression is naturally not independent of the land surface emissivity. As a result, prior to the rainfall estimation, different screening approaches are commonly employed to properly exclude depressions caused by the background noise (e.g., snow and desert surfaces). Among these, the early version of the GPROF [23], [24] suggests static thresholding (22–85 GHz $>$ 8 K) to detect the raining signatures of the spectral brightness temperatures measured by the TRMM microwave imager (TMI). A more involved scattering index has been also suggested in [28] and [29], which has been partly used to develop the launch version of the land retrieval algorithm for the Advanced Microwave Scanning Radiometer–Earth Observing System (AMSR-E) [18].

Since the successful launch of the TRMM satellite, a major body of research has been also devoted to developing rainfall retrieval algorithms by exploiting the coincident observations provided by the TMI and the TRMM precipitation radar (PR) (e.g., see [30]–[36]). The basic idea has been focused on combining, in an optimal sense, the information content of both sensors for obtaining improved estimates of the rainfall profile and, perhaps, the microphysical properties of the atmospheric constituents. Typically, these methods use a variational cost function to reconcile the observations provided by both instruments [33]–[36]. Recently, Kummerow *et al.* [25] have combined the PR data with the physically driven database of the GPROF algorithm to make the database more observationally consistent. Using coincident TMI and PR observations and principal component analysis (PCA), a low-dimensional approximation method is introduced in [14] and [37], which is known as the University of Wisconsin algorithm. This algorithm suggests a PCA-based approach to project the nine TMI channels onto three pseudochannels for filtering the background noise and reducing redundancies in the TMI channels. These pseudochannels are then used within a matching process to efficiently retrieve surface rain rates using a compactly designed *a priori* database in a Bayesian context.

Passive rainfall retrieval remains a challenge particularly for: 1) the detection and estimation of light rainfall over land and adjacent to coastlines; 2) the unbiased estimation of rainfall over highly emissive and nonhomogeneous land surfaces; and 3) the probabilistic recovery of the small-scale features of rainfall extremes both over land and ocean (see [14] and [38] and the references therein). In this paper, motivated by these continuous challenges, we introduce a new Bayesian retrieval algorithm, which is called the shrunken locally linear embedding algorithm for retrieval of precipitation (ShARP). This retrieval algorithm is guided by *a priori* collections of spectral radiances and their corresponding rainfall profiles, which are the so-called spectral and rainfall "dictionaries." The core part is inspired by the concept of locally linear embedding [39], which assumes that "similar" spectral radiances and their corresponding rainfall profiles live close to two joint smooth manifolds, allowing locally linear approximations. To retrieve rainfall, ShARP uses a k-nearest-neighbor classification (detection step) coupled with a modern shrinkage regularization scheme (estimation step). For an observed spectral radiance, the detection step finds similar signatures in the spectral dictionary and decides whether the observed spectral radiance is nonraining or raining. For a raining spectral radiance, the estimation step uses a shrinkage estimator to obtain its representation coefficients in the spectral dictionary. Then, the representation coefficients are used to combine the corresponding rainfall profiles from the rainfall dictionary to retrieve the rainfall values of interest.

In summary, the main contribution and advantageous features of this algorithm for addressing the aforementioned retrieval challenges are as follows. First, the use of a supervised nearest neighbor classification results in minimal sensitivity to the variability of the underlying land surface emissivity. This property promises improved retrieval over troublesome surfaces and coastal zones without any dependence to other ancillary data. Second, the core estimation step makes use of a modern constrained regularization scheme, giving rise to sufficiently stable retrievals with reduced error compared with the classic least squares solutions. Third, by design and due to the used regularization scheme, the algorithm is flexible and robust enough to employ dictionaries populated empirically, via physically based modeling, or a combination of them. Fourth, the algorithm allows us to approximate the posterior probability density function of the retrieved rainfall, which is particularly useful for the hazard assessment of rainfall extremes and their hydrogeomorphic impacts. It is important to note that the current implementation of our algorithm is fully empirical as we only populate the rainfall and spectral dictionaries with the coincident observations of the TRMM-PR and the TMI. Therefore, in the absence of any independent ground-based validation, all of the presented retrieval results are bounded by the accuracy of the PR sensor/algorithm [40]. Clearly, as we validate our results with 2A25, improved retrievals do not often come as a surprise; however, they remain of significant importance as the passive retrieval methods are currently empirical over land and coastal areas.

Section II is devoted to explaining the rainfall data set and studying the rainfall spectral patterns relevant to the design of the presented algorithm. Section III explains the details of ShARP. Using the TRMM data, in Section IV, some retrieval results are presented and compared with the currently operational PR-2A25 and TMI-2A12 retrieval products (version 7). Conclusions are drawn and future lines of research are pointed out in Section V.

II. TRMM Rainfall Database

Before we embark upon a detailed algorithmic discussion, we provide a brief explanation of the data set used and some

relevant insights into the structure of raining and nonraining microwave spectral patterns, which are essential to the development of our algorithm.

The TRMM-PR is a Ku-band radar that operates in a single polarization mode at a frequency of 13.8 GHz. After the TRMM boost, the PR provides direct measurements of rainfall reflectivity at a grid size of ∼5 km every ∼250 m of the troposphere at nadir, over a swath width of 247 km. On the other hand, the TMI is a dual-polarized multichannel radiometer that operates on central frequencies of 10.65, 19.35, 21.3, 37.0, and 85.5 GHz. All of the channels are horizontally and vertically polarized, except the vertical water vapor channel at 21.3 GHz. During the postboost era, the TMI provides spectral brightness temperatures over a swath width of 878 km, with different spatial resolutions of 72 km × 43 km, 35 km × 21 km, 26 km × 21 km, 18 km × 10 km, and 8 km × 6 km at the aforementioned central frequencies, respectively. By design, the TMI and PR sensors provide overlapping observations over the inner swath within the radar field of view at different resolutions. A thorough exposition of the TRMM sensor packages can be found in [41].

Here, we use the coincident 2A25 (level II) product of the radar profiling algorithm [42] and the 1B11 (level I) product of the radiometer to construct the rainfall and spectral dictionaries. To register all of the data onto a single grid of latitude/longitude, we used nearest neighbor interpolation and mapped the TMI spectral temperatures onto the reported PR grids. Note that, in this case, we neither lose nor add any information and retrieve rainfall at the native resolution of the 1B11 product at the 85-GHz high-frequency channel. Clearly, in this resolution, the lower frequency channels provide redundant spectral information over neighboring grid boxes, whereas their combinations with higher frequency channels may still provide distinct multispectral information. Accordingly, throughout this paper, we use a large collection of collocated TMI and PR data, which is hereafter called the "rainfall database" over the TRMM inner swath for all orbital tracks in calendar years 2002, 2005, 2008, 2011, and 2012.

Using the collected rainfall database, Fig. 1 shows the conditional expectations of the TMI spectral brightness temperatures for different ranges of the PR rainfall intensities and their coefficients of variation. Specifically, each column of the shown images demonstrates the conditional mean of the TMI channels, whereas each row shows the average response of the channels to the underlying rainfall variability. The stem plots represent the coefficients of variation of the brightness temperatures for each channel. Over ocean (top panel), we see that almost all frequencies are relatively responsive to the underlying surface rainfall variability. Horizontal channels of 10 and 19 GHz show the maximum normalized variations, whereas the vertical polarizations in frequencies of 21 and 37 GHz are the least responsive channels. This observation is consistent with the fact that the ocean surface is less emissive in horizontal polarizations for the TMI view angle, giving rise to a colder background and, thus, a larger signal-to-noise ratio of the raining signatures [43]. On the contrary, over land, almost all of the low-frequency channels below 21 GHz show relatively small coefficients of variation compared with the higher frequencies. It will be clear later on that these coefficients of variation can be used to properly weight each channel to better guide the proposed retrieval approach. Therefore, for each sampled $\mathbf{y}$, it can be naturally concluded that a properly chosen statistic of $\{r_k(\mathbf{y})\}_{k=1}^{K}$ in the following form may be adopted as a stable estimator of x:

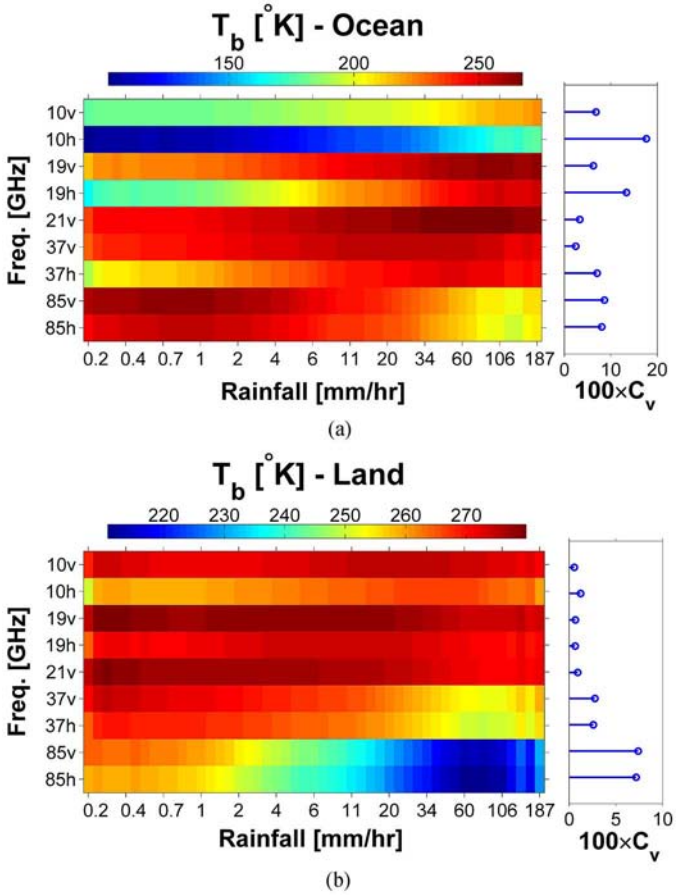

Fig. 1. Expected values of the spectral brightness temperatures for different intervals of the surface rainfall intensity over (top panel) ocean and (bottom panel) land. The images are inferred from coincident pairs of the TMI-1B11 and PR-2A25 products obtained from 1000 randomly chosen orbits in our rainfall database. The stem plots demonstrate the coefficients of variation for each spectral band in response to the underlying rainfall variability. Note that the rainfall intervals on the x-axis are logarithmically spaced between 0.2 and 200 mm/h.

$$\hat{x} = \sum_{k=1}^{K} c_k \, r_k(\mathbf{y}) \tag{1}$$

where c_k denotes some optimal coefficients.

Furthermore, to better understand the correspondence between the neighboring raining spectral brightness temperatures, in the Euclidean sense, and their surface rainfall intensities, we independently collected two learning sets of the form $\mathcal{L} = \{(\mathbf{b}_i, r_i)\}_{i=1}^{M}$ over ocean and land. Each set contains $M \approxeq 10^6$ of coincident 1B11 spectral brightness temperatures $\mathbf{b} \in \Re^9$ and their corresponding 2A25 surface rainfall $r \in \Re$ estimates. From a mathematical standpoint, a simple nearest neighbor search reveals that the spectral temperatures over ocean and

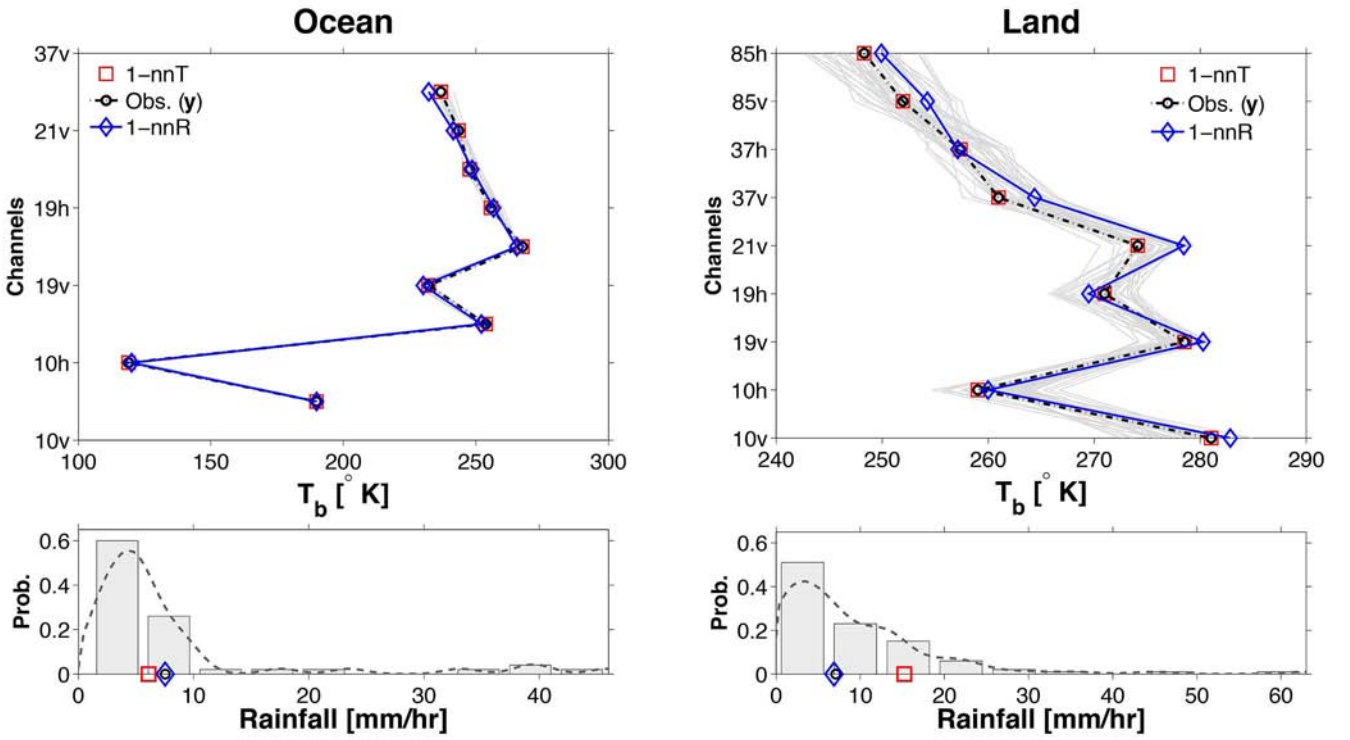

Fig. 2. (Top panels) Two arbitrary sampled raining vectors of the TMI-IB11 spectral brightness temperatures (dotted black lines with circles) over (left) ocean and (right) land. The gray lines are the 50-nearest spectral neighbors in the Euclidean sense, which are obtained from an independent learning set of the TMI-1B11 observations. (Bottom panels) PR-2A25 surface rainfall probability histograms of the 50 spectral neighbors, as shown in the top panels. In the top and bottom panels, the red squares and the blue solid lines with diamonds show the 1-nearest neighbor in the spectral (1-nnT) and rainfall (1-nnR) spaces, respectively.

land are not uniquely related to the estimated surface rainfall intensities in the Euclidean sense (for more discussion, see [44]). Nevertheless, in the known lack of uniqueness, a basic question arises: How can we obtain "stable" estimates of the surface rainfall using neighboring spectral brightness temperatures in a properly collected learning set? To this end, let us assume that a spectral vector of brightness temperature is denoted by $\mathbf{y}$ and that its scalar surface rainfall value of interest is x. The top panels from left to right in Fig. 2 demonstrate two arbitrary vectors of the 1B11 raining brightness temperatures $\mathbf{y} \in \Re^9$ (black dashed lines) over ocean and land, together with their 50 nearest neighbors $\{\mathbf{b}_k(\mathbf{y})\}_{k=1}^{K=50}$ (gray solid lines) obtained from the collected learning sets. The bottom panels show the corresponding surface rainfall values $\{r_k(\mathbf{y})\}_{k=1}^{K=50}$ and their probability histograms. It turns out that all of the 50 nearest spectral brightness temperatures were raining, except for only one of them over land. This observation implies that a supervised nearest-neighbor classification, using coincident TMI and PR data, might be a very powerful approach for the rain/no-rain discrimination problem. Furthermore, it can be seen that the first nearest neighbor in the spectral space (1-nnT) does not necessarily relate to the nearest neighbor (1-nnR) in the rainfall space. However, in both cases, the surface rainfalls of the neighboring spectral vectors are bounding the rainfall values x of interest. These bounds, both in the spectral and rainfall spaces, are clearly tighter over ocean than over land mainly due to the stronger signal-to-noise ratio of the rainfall signatures.

III. ShARP

A. Rainfall Retrieval as Inverse Problem

Passive rainfall retrieval in the microwave bands can be considered a nonlinear inverse problem, where its solution shall be constrained by the underlying laws of atmospheric thermal radiative transfer in a weak or strong sense [45]. By a strong sense, we mean that the retrieved rainfall profile shall be exactly consistent with the underlying physics, whereas in a weak sense, some bounded errors are admissible. To recast the microwave rainfall retrieval in a standard form of a discrete inverse problem, let us assume that each vector of the spectral brightness temperatures and their corresponding rainfall profiles are $\mathbf{y} = (y_1, y_2, \ldots, y_{n_c})^T$ and $\mathbf{x} = (x_1, x_2, \ldots, x_{n_r})^T$, respectively, where n_c and n_r denote the number of spectral channels and the number vertical layers of the rainfall intensity profile, respectively. As a result, in a finite dimension, spectral observations might be related to the rainfall intensity profile through the following nonlinear observation model:

$$\mathbf{y} = \mathcal{F}(\mathbf{x}) + \mathbf{v} \tag{2}$$

where $\mathcal{F}(\cdot): \mathbf{x} \rightarrow \mathbf{y}$ can be considered a functional representation of the radiative transfer equations that maps the rainfall intensity profiles onto the space of the spectral brightness temperatures, and $\mathbf{v} \in \Re^{n_c}$ represents the observation error with finite energy. Obviously, the goal of the retrieval is to obtain an estimate of rainfall profile $\mathbf{x}$, given spectral brightness

temperatures $\mathbf{y}$, the radiative transfer functional $\mathcal{F}(\cdot)$, and the *a priori* information about the error. The search for a stable closed-form solution to the aforementioned inverse problem seems infeasible, at least for now, given the fact that $\mathcal{F}(\cdot)$ is extremely nonlinear, particularly under the scattering dominant regime. In the following section, it will be clear that our algorithm provides a solution to this complex inverse problem in a weak sense.

B. Algorithm

Motivated by our observations in Section II, to bridge the explained complexities in the rainfall retrieval problem, our algorithm relies on an *a priori* collected database denoted by $\mathcal{L} = \{(\mathbf{b}_i, \mathbf{r}_i)\}_{i=1}^{M}$. This set is populated by a large number of coincident brightness temperatures $\mathbf{b}_i = [b_{1i}, b_{2i}, \ldots, b_{n_c i}]^T \in \Re^{n_c}$ and their corresponding rainfall profiles $\mathbf{r}_i = [r_{1i}, r_{2i}, \ldots, r_{n_r i}]^T \in \Re^{n_r}$. For notational convenience, let us stack these pairs according to a fixed order in two joint matrices $\mathbf{B} = [\mathbf{b}_1 | \ldots | \mathbf{b}_M] \in \Re^{n_c \times M}$ and $\mathbf{R} = [\mathbf{r}_1 | \ldots | \mathbf{r}_M] \in \Re^{n_r \times M}$, which are called the spectral and rainfall "dictionaries," respectively. In our notation, each of these pairs are called elementary "atoms" to be used for the reconstruction of the rainfall fields from their observed spectral signatures. As is evident, these dictionaries can be populated either by observational or physically based generated pairs.

In the detection step, we simply use a supervised nearest-neighbor classification rule, which is guided by the dictionaries. In particular, for a given observation vector of spectral brightness temperature $\mathbf{y} \in \Re^{n_c}$ and dictionary pair $(\mathbf{B}, \mathbf{R})$, let us assume that $\mathcal{S}$ denotes the set of K column indexes of $\mathbf{B}$ that contain the nearest spectral atoms to $\mathbf{y}$ in the Euclidean sense. Given this set, the algorithm forms two joint subdictionaries $(\mathbf{B}_\mathcal{S} \in \Re^{n_c \times K}, \mathbf{R}_\mathcal{S} \in \Re^{n_r \times K})$, which are generated by those $K = |\mathcal{S}|$ nearest spectral $\{\mathbf{b}_k\}_{k=1}^{K} \in \mathbf{B}$ and their corresponding rainfall atoms $\{\mathbf{r}_k\}_{k=1}^{K} \in \mathbf{R}$. Assuming that the last row of rainfall subdictionary $\mathbf{R}_\mathcal{S}$ contains the near-surface rainfall intensity values, the algorithm simply makes use of a probabilistic vote rule to declare $\mathbf{y}$ as raining or nonraining. In other words, choosing a probability threshold p, the algorithm labels $\mathbf{y}$ as raining if more than pK number of $\{\mathbf{r}_k\}_{k=1}^{K}$ are raining at the surface. In the estimation step, motivated by the results in Fig. 2, we assume that the true rainfall profile $\mathbf{x}$ of the given spectral observation $\mathbf{y}$ can be well explained by the $\mathbf{R}_\mathcal{S}$ atoms through the following linear model:

$$\mathbf{x} = \mathbf{R}_\mathcal{S}\mathbf{c} + \mathbf{e} \tag{3}$$

where $\mathbf{c} \in \Re^K$ is a vector of the representation coefficients that linearly combines the atoms of the rainfall subdictionary, and $\mathbf{e} \in \Re^{n_r}$ denotes a zero mean error with finite energy. As a result, given an estimate of the representation coefficients $\hat{\mathbf{c}}$, the conditional expectation of the rainfall profile $\hat{\mathbf{x}}$ can be obtained as follows:

$$\hat{\mathbf{x}} = \mathbb{E}(\mathbf{x}|\hat{\mathbf{c}}) = \mathbf{R}_\mathcal{S}\hat{\mathbf{c}}. \tag{4}$$

Obviously, the estimation of the representation coefficients solely from (3) is ambiguous as both sides of the equation are unknown. To find a solution, as previously explained, we assume that the neighboring rainfall profiles and their spectral signatures live close to two smooth manifolds with analogous geometric structures and, thus, similar locally linear representations. Therefore, the algorithm assumes a spectral observation model with the same linear representation coefficients as follows:

$$\mathbf{y} = \mathbf{B}_\mathcal{S}\mathbf{c} + \mathbf{v} \tag{5}$$

where $\mathbf{v} \in \Re^{n_c}$ denotes a zero mean error with finite energy. As is evident, the estimation of the representation coefficients from (5) is no longer an ill-defined problem. To estimate the representation coefficients in this linear model, the weighted minimum-mean-square-error estimator, which is constrained to the probability simplex, seems to be the first choice as follows:

$$\begin{aligned} \underset{\mathbf{c}}{\text{minimize}} \quad & \left\| \mathbf{W}^{1/2}(\mathbf{y} - \mathbf{B}_\mathcal{S}\mathbf{c}) \right\|_2^2 \\ \text{subject to} \quad & \mathbf{c} \succeq 0,\ \mathbf{1}^T\mathbf{c} = 1 \end{aligned} \tag{6}$$

where the ℓ_2-norm is $\|\mathbf{c}\|_2^2 = \Sigma_i c_i^2$, $\mathbf{c} \succeq 0$ implies the element-wise nonnegativity, and the positive definite $\mathbf{W} \succ 0$ in $\Re^{n_c \times n_c}$ determines the relative importance or weights of each channel. These weights may be chosen to relatively encode the signal-to-noise ratio of the spectral raining signatures. Note that the nonnegativity constraint is required to be physically consistent with the positivity of the brightness temperatures in degree of Kelvin. Furthermore, the sum to one constraint assures that the estimates are locally unbiased. More importantly, this equality constraint makes the solution invariant to the rotation, rescaling, and translation of the neighboring spectral observations [39]. For a similar concept in rainfall downscaling, see [46] and [47].

However, problem (6) is likely to be severely ill posed due to the observation noise, particularly when the column dimension of $\mathbf{B}_\mathcal{S}$ is larger than that of spectral bands n_c. To make the problem well posed and sufficiently stable, we suggest the following regularization scheme:

$$\begin{aligned} \underset{\mathbf{c}}{\text{minimize}} \quad & \left\| \mathbf{W}^{1/2}(\mathbf{y} - \mathbf{B}_\mathcal{S}\mathbf{c}) \right\|_2^2 + \lambda_1\|\mathbf{c}\|_1 + \lambda_2\|\mathbf{c}\|_2^2 \\ \text{subject to} \quad & \mathbf{c} \succeq 0,\ \mathbf{1}^T\mathbf{c} = 1 \end{aligned} \tag{7}$$

where the ℓ_1-norm is $\|\mathbf{c}\|_1 = \Sigma_i |c_i|$, and λ_1, λ_2 are nonnegative regularization parameters. Obviously, by obtaining $\hat{\mathbf{c}}$ as the solution of the aforementioned problem, we can retrieve the rainfall using expression (4) as $\hat{\mathbf{x}} = \mathbf{R}_\mathcal{S}\hat{\mathbf{c}}$.

Note that problem (7) is a nonsmooth convex problem. It is nonsmooth as the ℓ_1-norm is not differentiable at the origin. Convexity arises as it uses a conic combination of two well-known convex penalty functions to regularize a classic weighted least squares problem over a convex set. These two regularization functions have been widely used to properly narrow down the solution of ill-posed inverse problems. In an underdetermined system of equations, the ℓ_1-norm penalty has proven to be an effective regularization for obtaining "sparse" solutions. In other words, it turns out that this regularization promotes sparsity in the solutions as it uses a minimal number of atoms of $\mathbf{B}_\mathcal{S}$ while retaining the maximum amount of information (e.g., see [48]–[51]). On the other hand, the ℓ_2-norm penalty is the most widely used regularization approach to

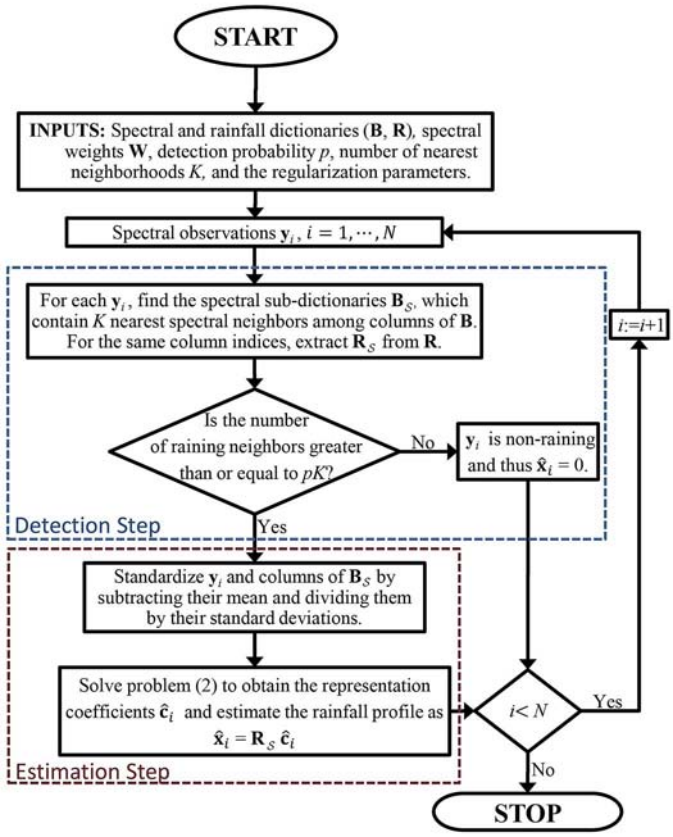

Fig. 3. Flowchart of ShARP. See Algorithm 1 for a more detailed explanation.

stabilize the solutions of "dense" ill-posed inverse problems while incorporating all the atoms of $\mathbf{B}_S$ in the solution (e.g., see [52] and [53]). Solely confining the regularization in (7) to the ℓ_1-norm ($\lambda_2 = 0$) is restrictive for rainfall retrieval in the current setting of our algorithm for two main reasons. First, the number of selected columns of $\mathbf{B}_S$ or, e.g., the nonzero elements of the representation coefficients will be bounded in this case by the number of available spectral bands n_c. Second, the spectral atoms in subdictionary $\mathbf{B}_S$ are likely to be highly correlated and clustered in groups. In this case, the ℓ_1-norm regularization typically fails to take into account the contribution of clustered atoms. On the other hand, all of the spectral atoms in $\mathbf{B}_S$ will be taken into account if we solely rely on the ℓ_2-norm penalty, which can lead to the selection of irrelevant atoms and overly smooth rainfall retrieval. However, the proposed mixed penalty removes the explained limitations of each individual regularization scheme through stabilizing the problem regularization path, encouraging grouping effects by shrinking the clusters of correlated atoms, and averaging their representation coefficients [54]. In addition, from a practical point of view, this mixed regularization increases the flexibility of the algorithm to cope with the ill conditioning arising due to the presence of very similar and correlated atoms in the spectral subdictionary. This property is extremely desirable particularly for the future developments of our algorithm to accommodate both observationally and physically generated dictionaries.

Throughout this paper, we consider a convex combination of regularization penalty functions by assuming that $\lambda_2 = \lambda\alpha$ and $\lambda_1 = \lambda(1-\alpha)$ for all $\alpha \in (0,1)$. As we use the concept of locally linear embedding together with the aforementioned mixed shrinkage estimation, we call our retrieval technique Shrunken locally linear embedding Algorithm for Retrieval of Precipitation (ShARP). The details are summarized in Algorithm 1 and sketched in Fig. 3. The given induced nonnegativity constraint in problem (7) allows us to solve it via constrained quadratic programming (QP) as follows:

$$\begin{aligned} \underset{\mathbf{c}}{\text{minimize}} \quad & \mathbf{c}^T \left(\mathbf{B}_S^T \mathbf{W} \mathbf{B}_S + \lambda_2 \mathbf{I}\right) \mathbf{c} + \left(\lambda_1 \mathbf{1} - 2\mathbf{B}_S^T \mathbf{W} \mathbf{y}\right)^T \mathbf{c} \\ \text{subject to} \quad & \mathbf{c} \succeq 0,\ \mathbf{1}^T \mathbf{c} = 1 \end{aligned} \tag{8}$$

where $\mathbf{1} = [1, \ldots, 1]^T \in \Re^K$.

Algorithm 1 Shrunken Locally Linear Embedding **A**lgorithm for **R**etrieval of **P**recipitation (ShARP).

Input: Spectral observations $\mathbf{Y}$ containing $\{\mathbf{y}_i = [y_{1i}, y_{2i}, \ldots, y_{n_c i}]^T \in \Re^{n_c}\}_{i=1}^N$ vectors of spectral brightness temperatures, spectral $\mathbf{B} \in \Re^{n_c \times M}$ and rainfall $\mathbf{R} \in \Re^{n_r \times M}$ dictionaries, weight matrix $\mathbf{W} \in \Re^{n_c \times n_c}$, detection probability p, the number of nearest neighbors K, and regularization parameters λ_1 and λ_2.
Output: Precipitation field $\mathbf{X}$ containing $\{\mathbf{x}_i \in \Re^{n_r}\}_{i=1}^N$ pixels of rainfall intensity profiles.
For $i := 1$ **to** N (step 1) **do**

- Find subdictionaries $\mathbf{B}_S \in \Re^{n_c \times K}$ and $\mathbf{R}_S \in \Re^{n_r \times K}$, where S is the set of the column indexes of $\mathbf{B}$ that contains the k-nearest neighbors of $\mathbf{y}_i$.
- Let $\mathbf{R}_S(\text{end}, :)$ denote the last row of $\mathbf{R}_S$ containing the neighboring surface rainfall.
- **If** $|\text{supp}(\mathbf{R}_S(\text{end}, :))| \geq pK$,
  - — Standardize $\mathbf{y}_i$ and the atoms of $\mathbf{B}_S$, such that $\sum_j^{n_c} y_{ji} = 0$, $\sum_j^{n_c} b_{jk} = 0$, and $\sum_j^{n_c} b_{jk}^2 = 1$, for $k = 1, \ldots, K$.
  - — Solve the following minimization:

$$\hat{\mathbf{c}}_i = \text{argmin}_{\mathbf{c}_i \succeq 0, \mathbf{1}^T \mathbf{c}_i = 1} \left\{ \left\| \mathbf{W}^{1/2} (\mathbf{y}_i - \mathbf{B}_S \mathbf{c}_i) \right\|_2^2 + \lambda_1 \|\mathbf{c}_i\|_1 + \lambda_2 \|\mathbf{c}_i\|_2^2 \right\}.$$

  - — $\hat{\mathbf{x}}_i = \mathbf{R}_S \hat{\mathbf{c}}_i$

else

  - — $\hat{\mathbf{x}}_i = 0$

End If
End For

It is important to note that problem (7) is, in effect, a constrained Bayesian MAP estimator under the following prior:

$$p(\mathbf{c}) \propto \exp\left(-\lambda_1 \|\mathbf{c}\|_1 - \lambda_2 \|\mathbf{c}\|_2^2\right) \tag{9}$$

which is a conic combination of the Gaussian and Laplace densities [54]. Therefore, the posterior density of the estimated

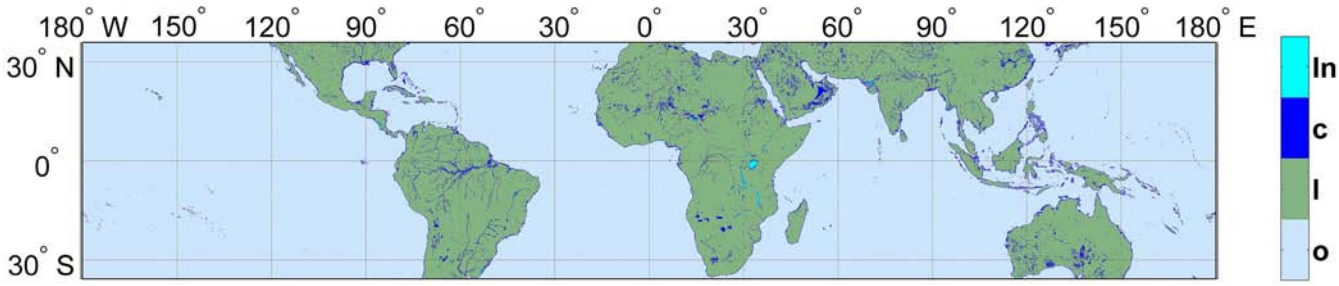

Fig. 4. Different Earth surface classes used in the current version of ShARP, i.e., inland water body (**In**), coastal zone (**c**), land (**l**), and ocean (**o**). The classification is adopted based on the available data (version 7) of the PR-1C21 product, which are mapped onto a 0.05° regular grid.

coefficients and, thus, the rainfall values are not Gaussian. As a result, the closed-form uncertainty analysis of the retrieved rainfall is not trivial and may be addressed through randomization or ensemble analysis. To this end, one can simply see that the rows of subdictionary $\mathbf{R}_S$ contain K samples of the posterior probability density function (pdf) of the neighboring rainfall intensity profiles. Thus, depending on the selected number of nearest neighbors, the whole posterior pdf of the ShARP estimator can be empirically approximated by counting the relative frequency of the rainfall occurrence. This strategy will be used in the sequel to estimate the uncertainty of the retrieved rainfall.

IV. Experiments Using TRMM Data

As previously explained, in the current implementation of ShARP, we confine our consideration to empirical rainfall and spectral dictionaries collected from the coincident PR-2A25 and TMI-1B11 products and only retrieve surface rainfall. Therefore, the 2A25 product can be used as a reference to validate the results of ShARP. To further examine the pros and cons of its performance, all of the retrieval experiments are also compared with the surface rainfall obtained from the standard passive TMI-2A12 retrieval product.

A. ShARP Setup

In the current implementation of ShARP, we defined four different earth surface classes, i.e., ocean, land, coast, and inland water (see Fig. 4). In other words, we collected four dictionaries over each surface class and use them in Algorithm 1 depending on the geolocation of a given pixel of the observed spectral brightness temperatures. This surface stratification is obtained from standard surface data in the PR-1C21 product (version 7) at a ~ 5 km $\times$ 5 km grid box. To construct the spectral and rainfall dictionaries, we randomly sampled 750 orbits from our rainfall database. In these sampled orbits, more than 25×10^6 pairs of raining and nonraining signatures were used to construct the required dictionaries.

1) Detection Step: As previously explained, rain/no-rain classification from microwave observations and its induced error on the quality of rainfall retrieval have been addressed in numerous studies [21], [27], [29], [54]–[56] and reported as a challenging problem that is not easy to mitigate, particularly over land [25]. Therefore, in developing rainfall retrieval techniques, we naturally have a choice to either first detect the storm raining areas and then estimate the rainfall intensities or just use an estimation scheme that automatically recovers the raining areas. In general, rainfall retrieval with a sequential rain/no-rain detection and estimation scheme may be advantageous in the sense that it allows us to control the probability of false alarm while only confining the computational expense of estimation to the detected raining areas.

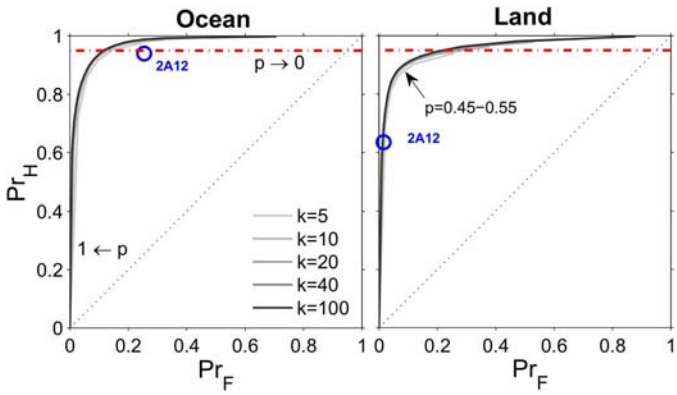

Fig. 5. Rainfall ROC curve over (left panel) ocean and (right panel) land for different probabilities of detection $p \in [0, 1]$ and numbers of nearest neighbors $K \in \{5, 10, 20, 40, 100\}$ of ShARP. The blue circles show the 2A12 (version 7) product, and the red dash-dotted lines show the 0.95 probability of hit as a datum.

TABLE I
Probability of Hit and False Alarm for 20 Nearest Neighbors $K = 20$ and a Probability Threshold of $p = 0.5$. The Results Are Obtained by Comparing ShARP With 2A25

		Observation (2A25)			
		Ocean		Land	
		rain	no-rain	rain	no-rain
ShARP	rain	0.96	0.08	0.90	0.06
	no-rain	0.04	0.92	0.1	0.94

Considering 2A25 as a reference rainfall field for the validation of ShARP, Fig. 5 shows the receiver operating characteristic (ROC) curve for the rain/no-rain detection step of our algorithm, as the classification parameters are varied. The ROC curve encodes the estimated probability of hit (Pr_H) versus the probability of false alarm (Pr_F). As is evident, the best classification algorithm yields a point at the upper left corner with $\mathrm{Pr}_H = 1$ and $\mathrm{Pr}_F = 0$. Here, the results are obtained by applying the detection step to more than 3×10^5 randomly chosen pixels of spectral observations from our rainfall database.

TABLE II
DIAGONAL ELEMENTS OF THE WEIGHT MATRIX $\mathbf{W} \in \Re^{9\times 9}$ USED IN ShARP FOR THE CHOSEN EARTH SURFACE CLASSES

Classes	Relative weights								
	Channels								
	10v	10h	19v	19h	21v	37h	37v	85v	85h
Ocean	0.39	1.00	0.35	0.76	0.19	0.14	0.40	0.49	0.45
Land	0.07	0.17	0.09	0.09	0.12	0.37	0.35	1.00	0.97
Coast	0.19	0.42	0.13	0.36	0.07	0.26	0.20	1.00	0.95
In-water	0.33	0.66	0.36	0.84	0.20	0.26	0.59	1.00	0.88

Note that these spectral pixels are randomly selected from our rainfall database and have not been used in construction of the retrieval dictionaries. In Fig. 5, we can see that the ShARP classification rule is not very sensitive to the number of chosen nearest neighbors as all of the curves are hardly distinguishable from each other. The ShARP rain/no-rain detection quality for $K = 20$ and the majority vote rule, i.e., $p = 0.5$, is presented in Table I. This table explains that, over ocean and land, our algorithm matches the raining pixels of the 2A25 product in 96% and 90% of the cases, whereas the false alarm rate does not exceed 8% and 6%, respectively. Fig. 5 also shows the position of the 2A12 retrieval product. It is seen that given that 2A25 is raining over ocean, 2A12 is raining in 95% of the cases. On the other hand, we see that, in 20% of the cases, 2A12 detects raining areas that may have been missed by 2A25 and, thus, ShARP. Although the interpretation of this discrepancy is not central to the thrust of this paper, this result seems to be consistent with the recent evidence from the CloudSat satellite suggesting that the PR underestimates the extent of light rain over ocean [57], which may reach up to 10% of the rainfall volume on average over the tropics [58]. Conversely, over land, we see that if 2A25 is raining, ShARP is raining in 90% of the cases, whereas 38% of these raining pixels are not captured in 2A12.

2) Estimation Step: After finding the storm raining areas, our algorithm moves toward the estimation of the rainfall intensities. Recall that we use a positive-definite weight matrix $\mathbf{W}$ in problem (7) that determines the relative importance of each channel over different surface classes. To design this weight matrix, we use the normalized coefficients of variation for each channel, as reported in Fig. 1. In particular, the relative weight of the ith channel for a specific surface class is obtained by normalizing its coefficient of variation as $w_i = c_v^i / \max_i(c_v^i)$, $i = 1, \ldots, 9$ (see Table II). The weight matrix is then assigned to be $\mathbf{W} = \text{diag}(w_i)$. Using these weights allows us to make the least squares term in problem (7) invariant to temperature translations among spectral channels and more responsive to a stronger rainfall signal-to-noise ratio. In other words, these weights reduce the saturation of the cost due to some excessively cold and/or warm channels while remaining sensitive to their relative variability. To solve problem (7), we use a primal–dual interior point method [59, Ch. 11]. Basically, in this class of convex optimization techniques, the inequality-constrained QP problem (8) is reformulated into an equality-constrained problem to which an iterative Newton's method can be applied. Specifically, we employed a QP interior-point-method solver in the MATLAB optimization package, which is based on a variant of the algorithm in [60]. In this optimization subalgorithm, the maximum number of iterations in Newton's steps is set to 200, and the termination tolerance on the function value and the magnitude of relative changes in the optimization variable are both set to $1e-8$. We set the algorithm regularization parameters to be $\lambda = 0.001$ and $\alpha = 0.1$, which appear to work well for a wide range of rainfall retrieval experiments. This setting permits the algorithm to perform full orbital rainfall retrieval on the order of 10–15 min on a contemporary desktop machine.

B. Instantaneous Retrieval Experiments

Figs. 6–8 demonstrate the results of few instantaneous retrieval experiments over ocean, land, and coastal areas, respectively. Here, we confined our consideration to some important storms recorded in the TRMM extreme event archives (http://trmm.gsfc.nasa.gov/publications_dir/extreme_events.html).

Over ocean, we used the TMI snapshots of hurricane Danielle (08/29/2010), super typhoon Usagi (09/21/2013), and tropical storm Helene (09/15/2006) (see Fig. 6). Over land, we focused on a few thunderstorms and mesoscale convective systems. These events include a squall line over Mali (08/29/2010), a local thunderstorm over Nigeria (06/28/1998), and a spring season squall line containing tornadic activities over Georgia, USA (01/30/2013) (see Fig. 7). Over coastal areas, we retrieved the TMI overpasses of tropical storm Fernand over the eastern coast of Mexico (08/26/2013), of hurricane Issac over Mississippi Delta, USA (08/28/2013 and 08/29/2012), and of typhoon Kai-tak over the Gulf of Tonkin, coastlines of Vietnam and southern China (08/17/2012) (see Fig. 8).

In general, our experiments in Figs. 6–8 demonstrate good agreement between the ShARP retrieval and the standard TRMM products. As previously noticed, we typically see that 2A12 retrieves much larger areas of light rain over ocean compared with 2A25 and, thus, with the current implementation of ShARP. We see that ShARP can properly recover the storm morphology and high-intensity and light rainfall both over ocean and land. For example, in the retrieval experiments of the tropical cyclones over ocean (see Fig. 6), the high-intensity rainfall cells, curvature, and multiband structure of the studied storms are well captured. Over land, in the retrieved thunderstorm over Nigeria (see the first row in Fig. 6) and the frontal system over Georgia (see the bottom row in Fig. 6), we see that the ordinary cells and stratiform trailing behind the leading edge of the squall line are well captured. Visual inspections of the retrieved rainfall at the ocean–land interface also confirm that the ShARP retrievals remain coherent over the interface and are in good agreement with the 2A12 and 2A25 products.

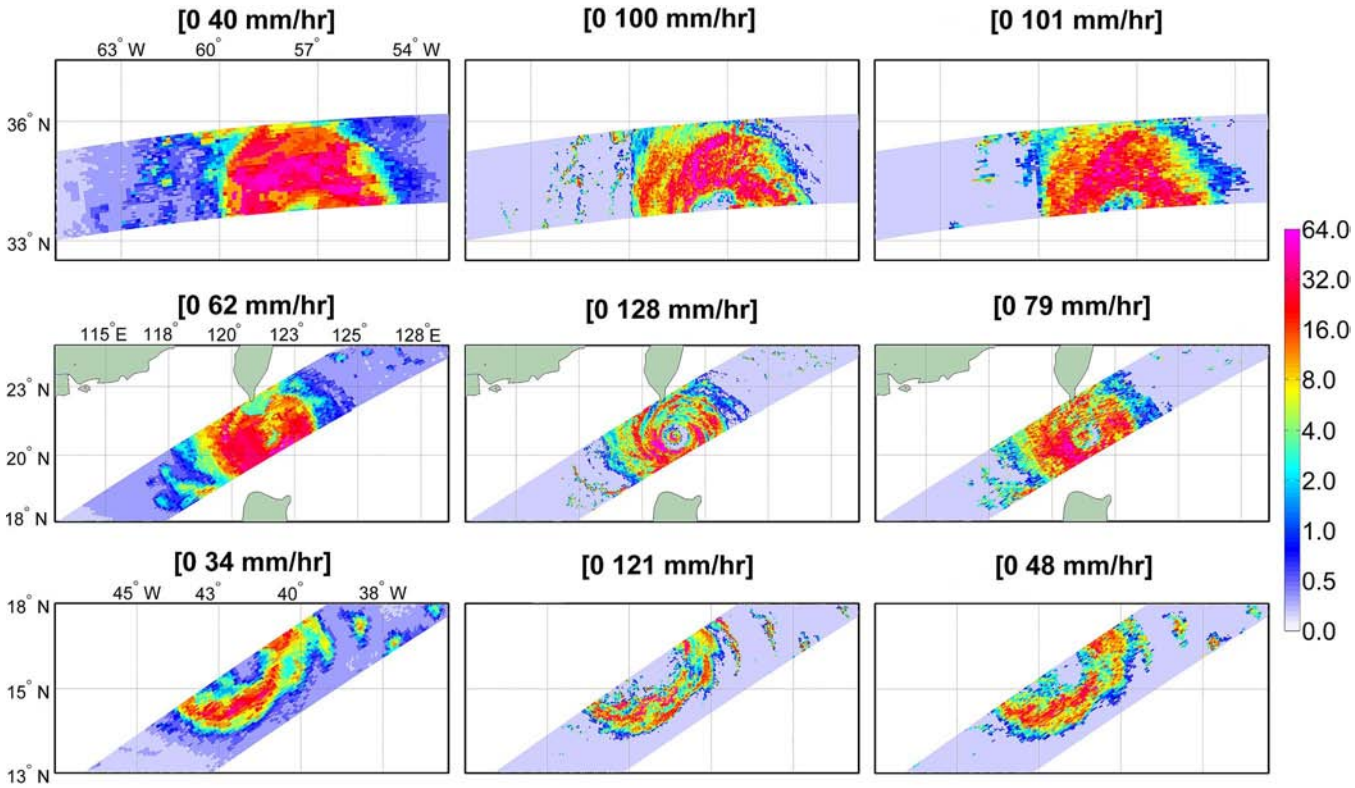

Fig. 6. (Left to right) TMI-2A12, PR-2A25, and ShARP retrievals. (Top to bottom panels) Hurricane Danielle in 08/29/2010 (orbit no. 72840) at 09:48 coordinated universal time (UTC), super typhoon Usagi in 09/21/2013 (orbit no. 90277) at 02:09 UTC, and tropical storm Helene in 09/15/2006 (orbit no. 50338) at 14:34 UTC.

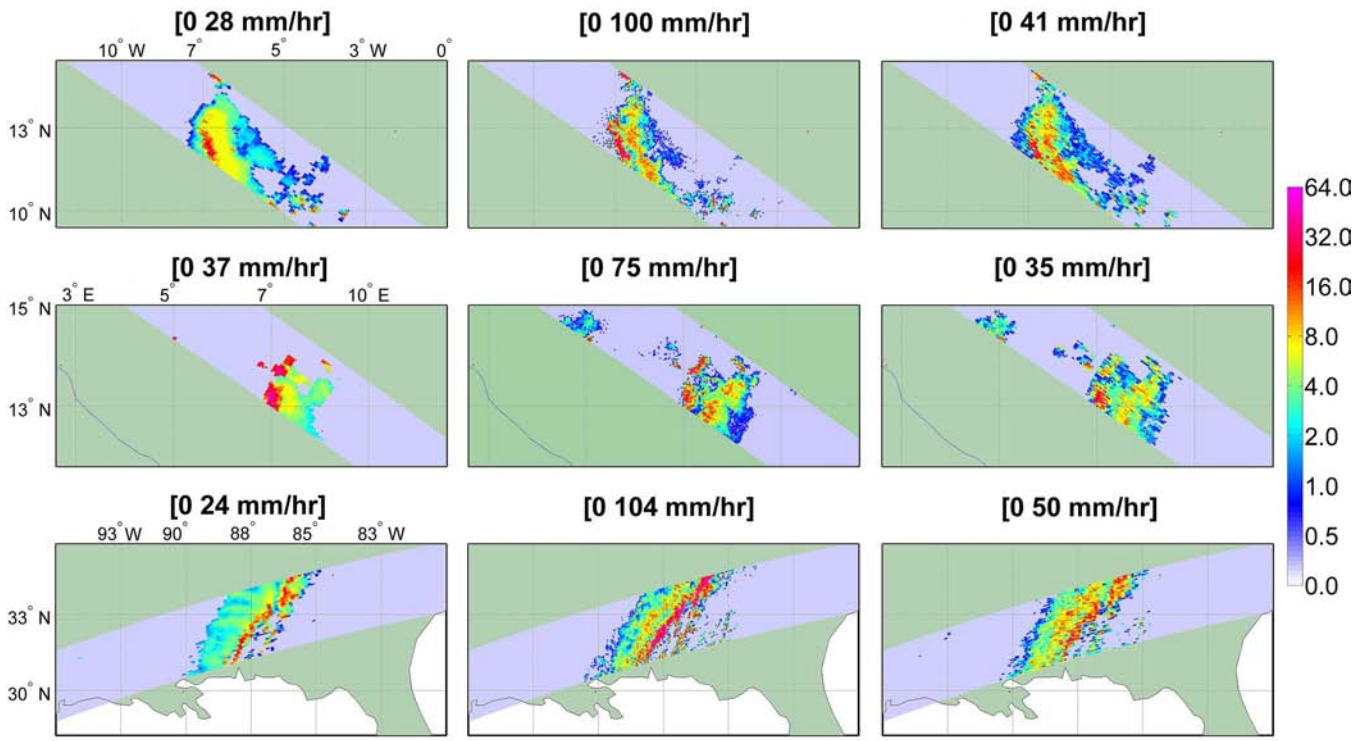

Fig. 7. (Left to right) TMI-2A12, PR-2A25, and ShARP retrievals. (Top to bottom panels) Thunderstorm over Mali, Africa, in 08/29/2010 (orbit no. 72841) at 10:30 UTC, summertime thunderstorm over Nigeria, Africa, in 06/28/1998 (orbit no. 03357) at 17:43 UTC, and spring season squall line of precipitation supercells and tornadoes over Georgia, USA, in 01/30/2013 (orbit no. 86639) at 16:22 UTC.

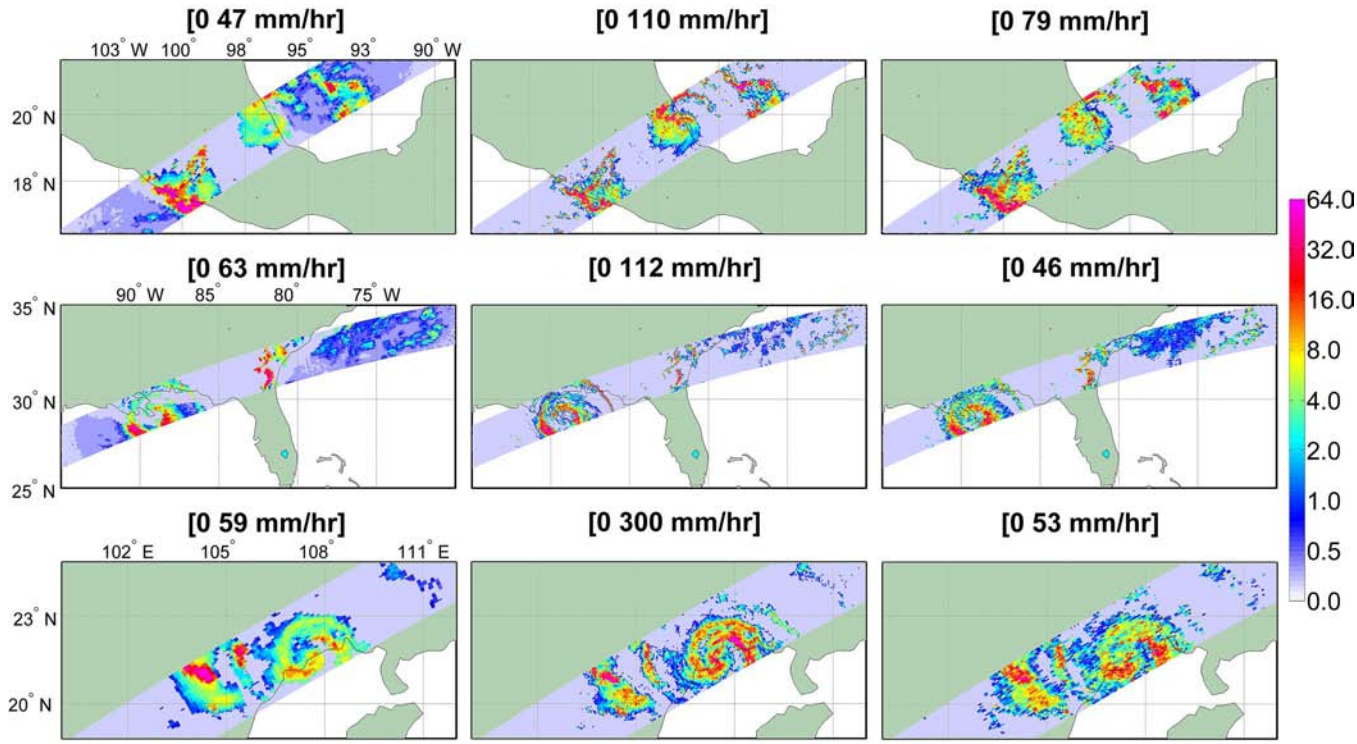

Fig. 8. (Left to right) TMI-2A12, PR-2A25, and ShARP retrievals. (Top to bottom panels) Tropical storm Fernand in 08/26/2013 (orbit no. 89874) at 05:30 UTC, hurricane Isaac in 08/28/2012 (orbit no. 84227) at 22:12 UTC, and typhoon Kai-tak in 08/17/2012 (orbit no. 84050) at 13:35 UTC.

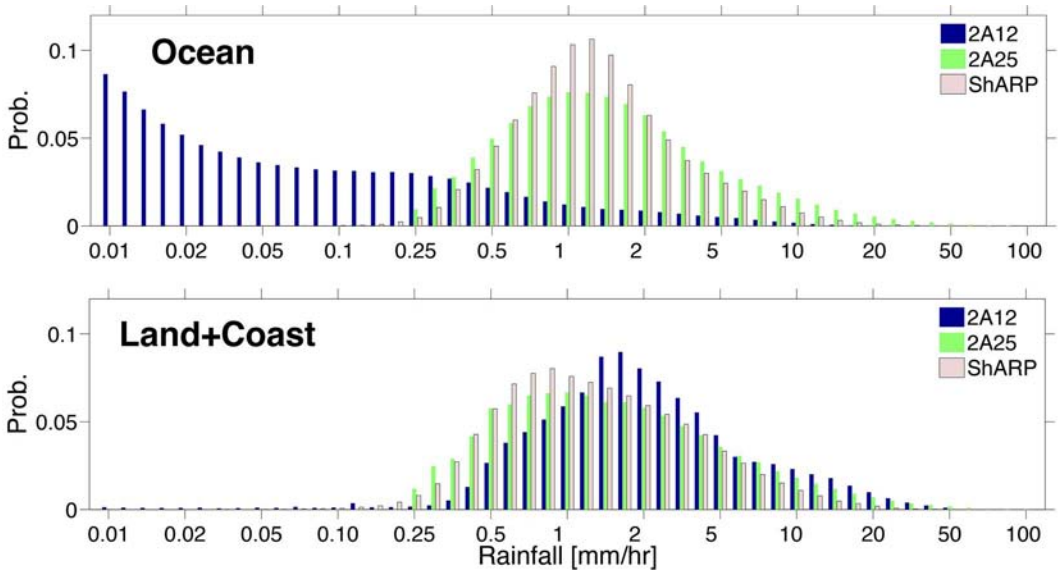

Fig. 9. Pixel-level probability histograms of the instantaneous rainfall retrievals ($> 1e + 6$ points for each product) for the TMI-2A12, PR-2A25, and ShARP products over the (top panel) ocean and (bottom panel) land–coast surface classes.

Fig. 9 compares the histogram of the retrieved rainfall values at the pixel level obtained from 100 randomly sampled TRMM orbits in calendar year 2013. Overall, it is shown that the distribution of ShARP and 2A25 are matched well. However, ShARP tends to retrieve more rain around the mode and falls a bit short over the tail. This behavior is expected as ShARP uses a MAP estimator that implicitly seeks the mode of the rainfall distribution. As previously noticed, over ocean, 2A12 retrieves much lower rain rates than the other two products. In 2A12, the highest probable range of rainfall intensity falls below 0.02 mm/h. In effect, more than 75% of the raining cases are reported to be below 0.25 mm/h, whereas the probability of rainfall at this range is almost zero in the other two products. In 2A25 and ShARP, 63% and 71% of the raining cases are within the range of 0.25–0.5 mm/h, respectively, whereas this probability is around 0.2 in 2A12. We see that the distribution of

TABLE III
RETRIEVAL DIFFERENCE METRICS OBTAINED BY COMPARING (a) ShARP VERSUS 2A25, (b) ShARP VERSUS 2A12, AND (c) 2A12 VERSUS 2A25 FOR 100 RANDOMLY CHOSEN ORBITAL TRACKS IN 2013. THE SHOWN STATISTICS ARE THE RMSD (IN MILLIMETERS PER HOUR), THE MAD (IN MILLIMETERS PER HOUR), AND SPEARMAN'S CORRELATION (ρ). THE STATISTICS ARE OBTAINED FOR INSTANTANEOUS RAINFALL ESTIMATES AT THE PIXEL-LEVEL OVER THE INTERSECTION OF THE RAINING AREAS OF ALL THREE RETRIEVAL PRODUCTS

Retrieval Difference Metrics						
Metrics	Surface Classes					
	Ocean			Land+Coast		
	(a)	(b)	(c)	(a)	(b)	(c)
RMSD	5.0	2.8	5.3	6.1	4.3	6.5
MAD	2.3	1.6	2.6	2.7	2.4	3.2
ρ	0.55	0.60	0.45	0.50	0.55	0.40

2A25 over ocean has the thickest tail among the others. In this product, the probability of rainfall exceeding 10 mm/h is $\sim$5%, whereas only 1.5% and 0.7% of the raining cases are in this range for ShARP and 2A12, respectively. Note that, as the PR is not the best indicator of light rainfall over the tropical ocean (e.g., see [61] and [62]), the interpretation of the recovered rainfall below the PR accuracy and its distribution in 2A12 cannot be explained in this paper and requires more thorough investigation. Over land and coastal areas, the rainfall distributions of all three products are more or less similar. The mode of the rainfall is around 0.9 mm/h in ShARP and 2A25, whereas the highest probable rainfall values are concentrated around 1.9 mm/h in 2A12. It is also apparent that 2A25 and, thus, ShARP detect more lower rain rates < 1 mm/h, whereas the detection of higher rain rates > 10 mm/h is more probable in 2A12 over land. It is important to note that, as the extent of raining areas are different in the studied retrievals, the observed differences in the probability distribution of instantaneous rainfall do not necessarily lead to large differences in the volumetric retrieved rainfall. In effect, we will show later on that the total annual estimates of rainfall match well in all three products.

To further validate the instantaneous retrieval of ShARP, we report the RMS difference (RMSD), the mean absolute difference (MAD), and Spearman's correlation ρ for each pair of the studied products. The computation of these proximity measures for instantaneous rainfall is not straightforward as these products do not share identical sets of raining areas. Table III shows the pixel-level estimates of these measures over the intersection of raining areas in the 100 randomly sampled orbits discussed in Fig. 9. As is evident, ShARP is closer and more correlated with 2A25 than with 2A12. Evaluating the pixel-level differences of the rainfall samples among the studied products shows that, typically, a large number of those deviations are very small, whereas a small number of them are typically very large. For instance, more than 55% of the differences between ShARP and 2A25 are less than 1 mm/h, whereas less than 5% of them are greater than 8 mm/h. This can be the main reason why the RMSD is almost twice that of the MAD metric in Table III. In effect, the RMSD can be easily saturated by a few large deviations as it quadratically penalizes them. On the other hand, the MAD linearly penalizes the differences and seems to be a more robust measure against a few numbers of large deviations.

As we explained, the posterior density of the ShARP retrievals can be empirically approximated via counting the frequency of rainfall occurrence in the atoms of the rainfall subdictionaries. Table IV reports a static estimation of the key percentiles of the posterior pdf for the examined 100 orbits. For brevity, we only present the results for the rainfall values falling between 0.1, 0.2, 0.5, 1, 2, 5, 10, 25, and 50 mm/h. Fig. 10 also shows some dynamic probability maps of the posteriori pdf for the snapshot of hurricane Danielle shown in Fig. 6. Clearly, this important feature of ShARP allows us to probabilistically perform rainfall retrieval and track the high-risk areas of the extreme rainfall based on a certain probability of exceedance.

C. Cumulative Experiments

To validate the results of our algorithm in a cumulative sense, we focus on all the orbital observations of the TRMM in 2013. To unify the sampling rate, we only use the available observations over the inner swath, where both sensors provide overlapping and validated rainfall observations. Fig. 11 demonstrates the annual rainfall estimates, which are mapped onto a $0.1^\circ \times 0.1^\circ$ grid. In general, we see good agreement between ShARP and the standard TRMM products. Here, as 2A25 potentially provides one of the best spaceborne estimates of the total rainfall volume over the tropics [58], we also study the deviations of the passive retrievals from this active product.

At a 0.1° resolution, the normalized RMSD (RMSD_n)[1] is about 36% and 48% for ShARP (see the bottom panel in Fig. 11) and 2A12 (see the top panel in Fig. 11), respectively. At a coarser resolution of the $1^\circ \times 1^\circ$ grid box, this metric reduces to 17% and 31% (see Fig. 12), whereas the overall correlation with 2A25 is 0.92 and 0.97 for 2A12 and ShARP, respectively (see Fig. 13). Zonal mean values are also presented in Fig. 14, with quantitative explanations in Table V. Over ocean, except in the North Atlantic midlatitude storm tracks, both ShARP and 2A12 slightly overestimate the total rainfall obtained from 2A25; most of the underestimation regions occur over land, particularly near coastal zones, islands, and peninsulas, although some overestimation can be seen in Central Africa and South America in both 2A12 and ShARP.

Fig. 12 shows that passive retrieval products overestimate ($\sim$300–400 mm) 2A25 on the narrow ridge of high precipitation in the Intertropical Convergence Zone (ITCZ) across the Pacific Ocean. As is evident, over the South Pacific, Atlantic, and Indian Ocean convergence zones, we also see some overestimation in ShARP, whereas the positive difference is relatively mitigated compared with the standard 2A12 product. In the North Atlantic midlatitude storm tracks, both passive retrievals slightly underestimate the annual rainfall, whereas the deviations are smaller in 2A12 compared with ShARP.

Some promising results of our algorithm seem to be over land and coastal zones. Over the subtropical hot desert, arid,

[1] RMSD_n is the RMSD, which is normalized by the square root of the sum of squared of the reference field at a pixel level.

TABLE IV
STATIC ESTIMATION OF KEY PERCENTILES (IN MILLIMETERS PER HOUR) OF THE POSTERIOR PDF OF THE ShARP RAINFALL RETRIEVALS FOR 100 SAMPLED ORBITS IN CALENDAR YEAR 2013. THE SECOND COLUMN DENOTES THE MEAN (IN MILLIMETERS PER HOUR) VALUES OF THE RETRIEVED RAINFALL WITHIN EACH BIN

Quantiles [mm/hr] of the ShARP Posterior PDF											
Bins	Mean	Ocean					Land + Coast				
		5th	25th	50th	75th	95th	5th	25th	50th	75th	95th
0.1-0.2	0.15	0.0	0.0	0.0	0.36	1.7	0.0	0.0	0.0	0.0	1.70
0.2-0.5	0.4	0.0	0.0	0.4	0.7	2.2	0.0	0.0	0.3	0.8	2.4
0.5-1.0	0.8	0.0	0.3	0.7	1.2	3.1	0.0	0.4	0.7	1.2	3.4
1.0-2.0	1.5	0.0	0.6	1.1	2.0	5.2	0.0	0.5	1.0	1.9	5.6
2.0-5.0	3.0	0.3	1.0	1.8	3.5	10.0	0.3	0.9	1.8	3.6	10.2
5.0-10.0	7.0	0.7	2.0	4.0	7.9	19.7	0.5	1.6	3.6	7.2	19.6
10.0-25.0	14.0	1.1	3.5	7.4	14.2	35.2	0.7	2.8	6.8	14.7	37.2
25.0-50.0	31.0	2.5	7.7	16.5	31.5	62.5	0.8	5.2	13.8	28.2	68.8

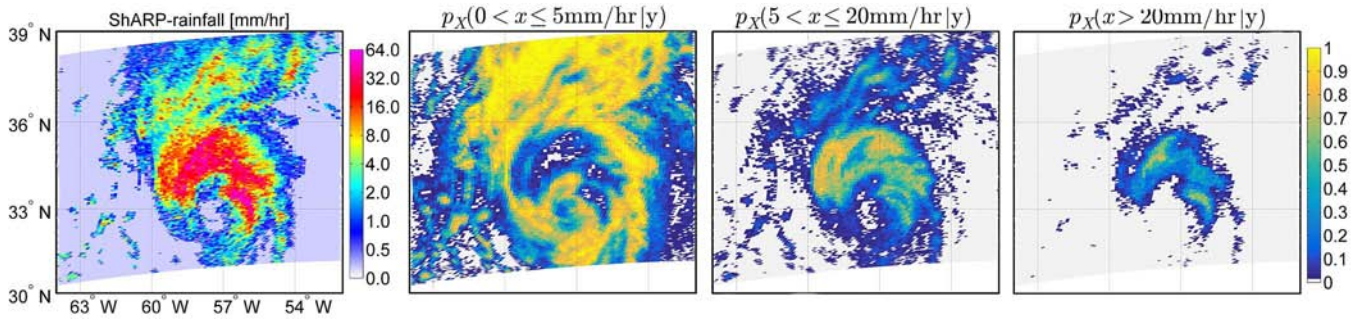

Fig. 10. Probability maps showing different segments of posterior pdf $p_X(x|y)$ for the (top left panel) ShARP retrieval of hurricane Danielle (orbit no. 72840) at 09:48 UTC.

and semiarid climates (e.g., Sahara, Arabian, Syrian deserts, and central Iran Plateau), we see that ShARP retrieves well the low rainfall amounts seen by the PR. Over Central Africa, both 2A12 and ShARP overestimate the 2A25 annual rainfall, whereas the gap seems to be smaller in ShARP. Over North America, it is seen that 2A12 shows good agreement with the PR estimates over the East Coast and Midwest of the USA. However, ShARP approximates well the PR over the West Coast and Southwest, where the rainfall signatures are predominantly corrupted with noise due to the highly emissive desert surfaces. Over South America, ShARP shows improved retrieval over Brazil and southern Amazon, whereas compared with 2A12, notable underestimation can be seen over the northern Amazon basin, Colombia, and Venezuela. Some improved results of our algorithm are over the snow-covered Tibetan highlands and Himalayas. We can see that ShARP can distinguish well the background noise from the rainfall signatures, and it reduces some overestimation seen in 2A12. Note that we have used the minimal number of Earth surface classifications and have not used any ancillary data (e.g., surface temperature) over the Tibetan Plateau. Indeed, due to the 9-D nearest neighbor selection of the spectral subdictionaries, our algorithm is apparently capable of robustly eliminating a large portion of the physically inconsistent spectral candidates in the detection step. Over Southeast Asia, where the rainfall signatures are masked by a mixture of ocean and land surface background radiation regimes, both ShARP and 2A12 underestimate 2A25. However, the negative differences in ShARP are slightly reduced compared with 2A12, particularly over Indonesia, Malaysia, and the Philippines.

A comparison of the total annual zonal mean values (see the left panel in Fig. 14) shows that ShARP approximates well the average latitudinal rainfall distribution. We can see that ShARP reconstructs well the 2A25 product over ocean not only over the tropics but also over the midlatitudes, where stratiform rainfall is dominant (see the middle panel in Fig. 14). Over land, ShARP underestimates the zonal mean within a narrow band (latitudes 5° S–N) around the tropics, whereas it performs well over the subtropical climate zones (see the right panel in Fig. 14). This underestimation is mainly contributed by the ShARP poor retrieval skill over the northern part of South America. A quantitative comparison of these zonal profiles is presented in Table V.

To briefly evaluate the intraannual performance of our algorithm, particularly over land and coastal areas, we also focused on a three-month rainfall accumulation for the period from January to March (JFM) of 2013. We confined the spatial extent of our evaluation within latitudes 15°–35° N and longitudes 60°–120° W (see Fig. 15). The rainfall in the JFM period is mainly supplied by the moisture coming from the Pacific Ocean through the subtropical jet stream and is intensified where the extratropical lifting saturates the atmospheric column over the Gulf of Mexico. This mechanism typically causes heavy precipitation events over the southeast of the USA and the Gulf of Mexico, whereas it leaves the southwest relatively dry. Overall, we see that ShARP properly retrieves the high and

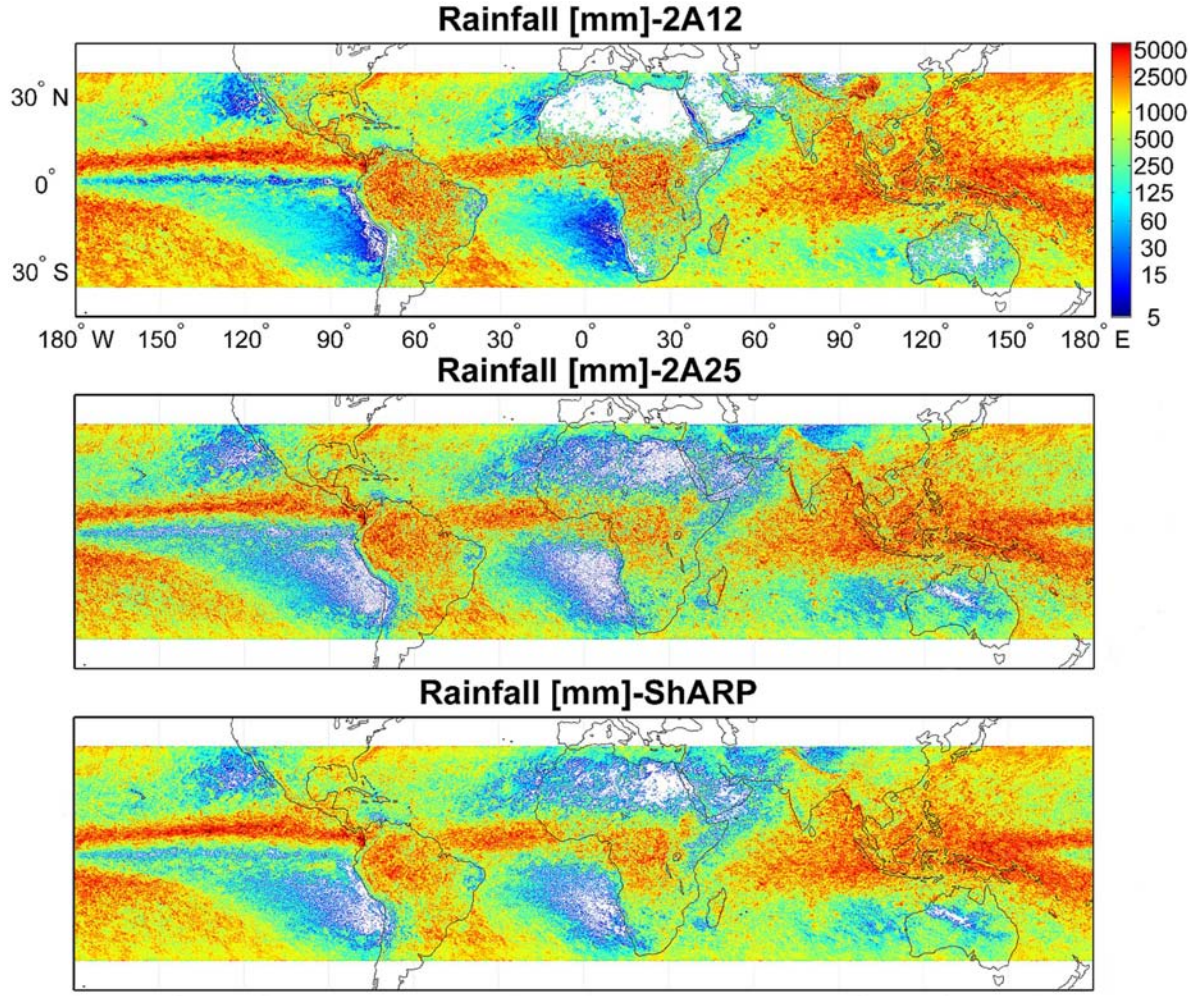

Fig. 11. Annual estimates of the total rainfall (in millimeters) in 2013 mapped onto a 0.1° grid box. (Top to bottom panels) 2A12, 2A25, and ShARP retrieval products.

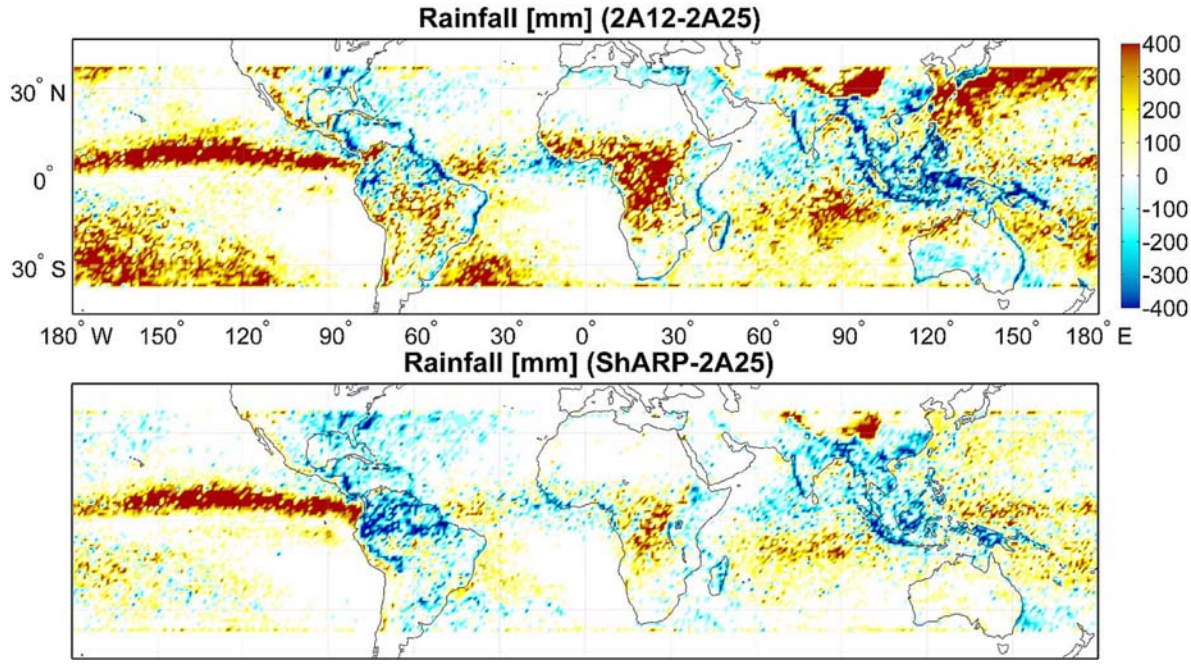

Fig. 12. Annual estimates of the total rainfall difference (in millimeters) for calendar year 2013. (Top to bottom panels) Difference between the 2A12 and ShARP retrievals with 2A25 at a grid size of $1^\circ \times 1^\circ$. Hot (red) and cold (blue) colors denote the intensity of the positive and negative differences, respectively.

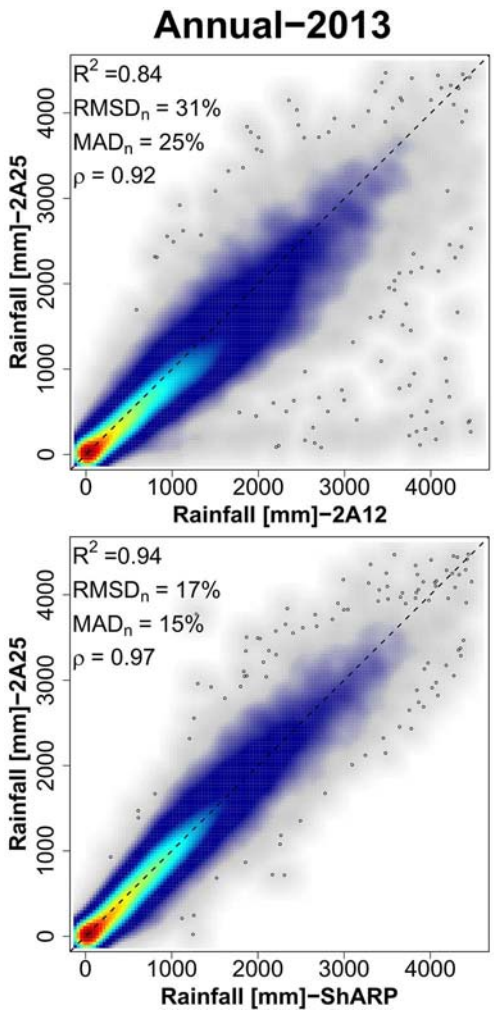

Fig. 13. Smooth scatter plots of the annual retrieved rainfall (in millimeters) by (top panel) 2A12 and (bottom panel) ShARP versus 2A25 at a grid size of $1^\circ \times 1^\circ$. Hot (red) and cold (blue) colors denote the higher and lower densities of the available rainfall intensity pairs, respectively. R^2 denotes the coefficient of determination, RMSD_n and MAD_n are the normalized RMSD and MAD, respectively, and ρ denotes the correlation coefficient.

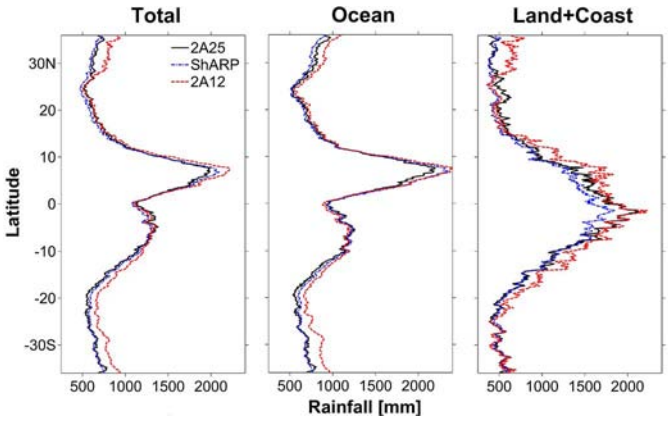

Fig. 14. Annual rainfall zonal mean values (in millimeters) obtained from the estimates of the annual rainfall shown in Fig. 11. (Left to right panels) Zonal mean values computed over all surface classes, ocean, and land–coasts.

low seasonal precipitation amounts in the JFM system, and its retrieved rainfall resembles well the standard TRMM products. Specifically, it is seen that, in the vicinity of the coast lines

TABLE V
RETRIEVAL SKILLS INCLUDING THE RMSD (IN MILLIMETERS) AND THE MEAN DIFFERENCE (IN MILLIMETERS) FOR THE ANNUAL ZONAL MEAN VALUES SHOWN IN FIG. 14

Product	Surface Class	Annual Zonal Mean	
		RMSD	MD
ShARP-2A25	Total	40.20	-6.53
	Ocean	47.61	7.15
	Land + Coast	95.67	-41.02
2A12-2A25	Total	103.04	73.63
	Ocean	99.50	69.42
	Land + Coast	37.62	79.43

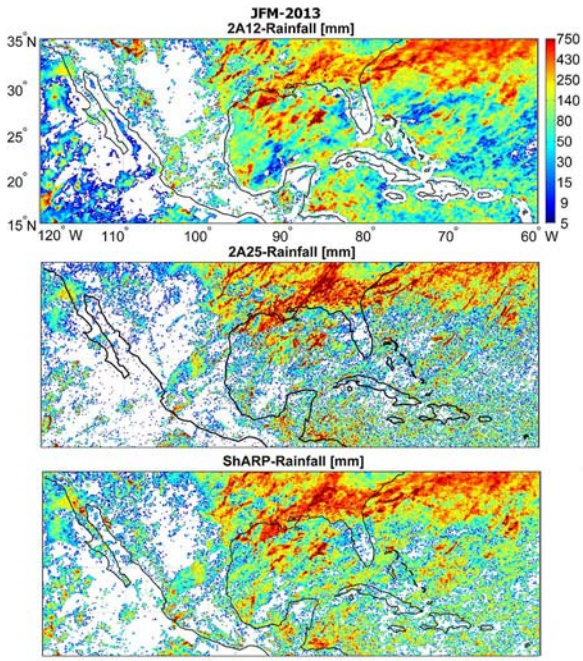

Fig. 15. Intraannual rainfall accumulation for the JFM period in 2013, mapped onto a 0.1° grid box.

of the Caribbean Islands and Bahamas, the lightrainfall values are captured well by ShARP. During this period, consistent with the instantaneous results shown in Fig. 5, the largest amount of raining areas over the ocean is detected by the 2A12 (88% of ocean), whereas this fraction is 71% and 66% in ShARP and 2A25, respectively. In contrast, ShARP detects the largest raining area (69%) over land, whereas this fraction is 63% and 50% in 2A25 and 2A12, respectively. The main factor contributing to the overestimation of 2A25 by ShARP is primarily due to the coarse resolution of the TMI sensor that is unable to resolve the signatures of small-scale precipitation events captured by the PR. A brief quantitative comparison of the JFM rainfall system, only over land and coastal areas, is presented in Fig. 16. As is evident, ShARP correlates well with 2A25, whereas we see some discrepancies showing that, for some light raining areas in 2A25, both ShARP and 2A12 retrieve high rainfall values. It turns out that some of these anomalies are due, in part, to the misinterpretation of the highly emissive ground as rainfall signatures. For example, we see that, over the Baja California Desert, ShARP exhibits overestimation spots, whereas the snow-covered land surface

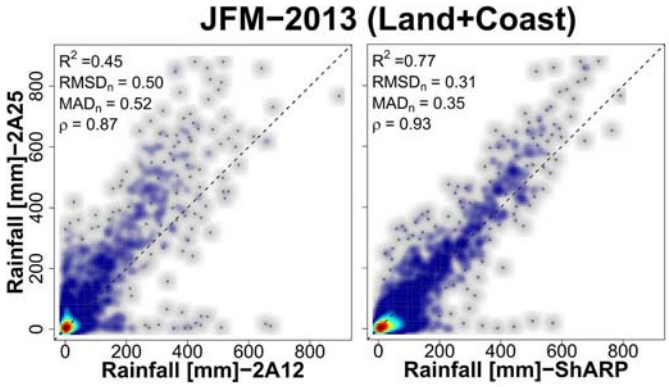

Fig. 16. Smooth scatter plots of the three-month rainfall accumulation (in millimeters), as shown in Fig. 15. The plots show (left panel) 2A12 and (right panel) ShARP versus 2A25 at a $0.5^\circ \times 0.5^\circ$ grid box. For explanations of the presented statistics, see the caption of Fig. 13.

in the month of January confuses the 2A12 algorithm over the northwest of Arizona ($\sim 110^\circ$ W, 35° N).

V. Concluding Remarks

We proposed a Bayesian microwave rainfall retrieval algorithm that makes use of *a priori* collected rainfall and spectral dictionaries. This algorithm relies on a nearest neighbor detection rule and exploits a modern shrinkage estimator. We have examined its performance using empirical dictionaries populated from coincident observations of the TRMM-PR and the TMI, and we demonstrated its considerable promise to provide accurate rainfall retrievals, particularly over land and coastal areas. In future research, the algorithm needs to be further verified for different rainfall regimes over ocean and land. Further efforts also need to be devoted to improving the retrieval of rainfall extremes both over land and ocean. Although we have confined our experiments to empirical dictionaries, the core of our algorithm is flexible and versatile enough to exploit both observational and physically based generated dictionaries. The proposed implementation is very parsimonious at this stage, and further refinements, such as smarter choices of surface classes by considering ground emissivity patterns and adding auxiliary state variables to the dictionaries (e.g., surface skin temperature and total column water), can definitely improve the performance of the proposed approach. Currently, we are developing a new version of this algorithm that uses compact dictionaries for faster and more accurate retrieval of the entire rainfall profile. The particular emphasis will be on the available spectral bands (10.65–183 GHz) of the radiometer and the observations of the dual-frequency PR aboard the successfully launched Global Precipitation Measuring satellites.

Acknowledgment

A. M. Ebtehaj would like to thank Prof. C. D. Kummerow of Colorado State University, Fort Collins, CO, USA, and Dr. F. J. Turk of the Jet Propulsion Laboratory for their comments and insightful discussions. The authors would like to thank the two anonymous reviewers for their comments. The TRMM 2A12 and 2A25 data were obtained through the anonymous File Transfer Protocol publicly available at ftp://trmmopen.gsfc.nasa.gov/pub/trmmdata.

References

[1] E. C. Barrett, "The estimation of monthly rainfall from satellite," *Monthly Weather Rev.*, vol. 98, no. 4, pp. 322–327, Apr. 1970.
[2] R. H. Blackmer, "Correlation of cloud brightness and radiance with precipitation intensity," Stanford Res. Inst. Menlo Park, CA, USA, Final Rep. –Task B (NEPRF TR8-75 (SRI)), 1975.
[3] B. J. Kilonsky and C. S. Ramage, "A technique for estimating tropical open-ocean rainfall from satellite observations," *J. Appl. Meteorol.*, vol. 15, no. 9, pp. 972–975, Sep. 1976.
[4] P. A. Arkin, "The relationship between fractional coverage of high cloud and rainfall accumulations during gate over the b-scale array," *Monthly Weather. Rev.*, vol. 107, no. 10, pp. 1382–1387, Oct. 1979.
[5] P. A. Arkin and P. E. Ardanuy, "Estimating climatic-scale precipitation from space: A review," *J. Climate*, vol. 2, no. 11, pp. 1229–1238, Nov. 1989.
[6] S. Lovejoy and G. Austin, "The delineation of rain areas from visible and IR satellite data for GATE and mid-latitudes," *Atmosp.-Ocean*, vol. 17, no. 1, pp. 77–92, 1979.
[7] K. Hsu, X. Gao, S. Sorooshian, and H. Gupta, "Precipitation estimation from remotely sensed information using artificial neural networks," *J. Appl. Meteorol.*, vol. 36, no. 9, pp. 1176–1190, Sep. 1997.
[8] S. Sorooshian *et al.*, "Evaluation of PERSIANN system satellite-based estimates of tropical rainfall," *Bull. Am. Meteorol. Soc.*, vol. 81, no. 9, pp. 2035–2046, Sep. 2000.
[9] T. T. Wilheit, A. T. C. Chang, M. S. V. Rao, E. B. Rodgers, and J. S. Theon, "A satellite technique for quantitatively mapping rainfall rates over the oceans," *J. Appl. Meteorol.*, vol. 16, no. 5, pp. 551–560, May 1977.
[10] G. Liu and J. A. Curry, "Retrieval of precipitation from satellite microwave measurement using both emission and scattering," *J. Geophys. Res., Atmosp.*, vol. 97, no. D9, pp. 9959–9974, Jun. 1992.
[11] G. W. Petty and K. B. Katsaros, "Precipitation observed over the South China sea by the Nimbus-7 scanning multichannel microwave radiometer during winter MONEX," *J. Appl. Meteorol.*, vol. 29, no. 4, pp. 273–287, Apr. 1990.
[12] G. W. Petty, "Physical retrievals of over-ocean rain rate from multichannel microwave imagery. Part I: Theoretical characteristics of normalized polarization and scattering indices," *Meteorol. Atmosp. Phys.*, vol. 54, no. 1–4, pp. 79–99, 1994.
[13] G. W. Petty, "Physical retrievals of over-ocean rain rate from multichannel microwave imagery. Part II: Algorithm implementation," *Meteorol. Atmosp. Phys.*, vol. 54, no. 1–4, pp. 101–121, 1994.
[14] G. W. Petty and K. Li, "Improved passive microwave retrievals of rain rate over land and ocean. 1. algorithm description," *J. Atmosp. Ocean. Technol.*, vol. 30, no. 11, pp. 2493–2508, Nov. 2013.
[15] R. W. Spencer, "A satellite passive 37-GHz scattering-based method for measuring oceanic rain rates," *J. Climate Appl. Meteorol.*, vol. 25, no. 6, pp. 754–766, Jun. 1986.
[16] T. Wilheit *et al.*, "Algorithms for the retrieval of rainfall from passive microwave measurements," *Remote Sens. Rev.*, vol. 11, no. 1–4, pp. 163–194, 1994.
[17] G. W. Petty and W. F. Krajewski, "Satellite estimation of precipitation over land," *Hydrol. Sci. J.*, vol. 41, no. 4, pp. 433–451, 1996.
[18] T. Wilheit, C. Kummerow, and R. Ferraro, "Rainfall algorithms for AMSR-E," *IEEE Trans. Geosci. Remote Sens.*, vol. 41, no. 2, pp. 204–214, Feb. 2003.
[19] W. S. Olson, "Physical retrieval of rainfall rates over the ocean by multispectral microwave radiometry: Application to tropical cyclones," *J. Geophys. Res.*, vol. 94, no. D2, pp. 2267–2280, Dec. 1989.
[20] A. Mugnai, E. A. Smith, and G. J. Tripoli, "Foundations for Statistical–Physical Precipitation Retrieval from passive microwave satellite measurements. Part II: Emission-source and generalized weighting-function properties of a time-dependent cloud-radiation model," *J. Appl. Meteorol.*, vol. 32, no. 1, pp. 17–39, Jan. 1993.
[21] C. Kummerow and L. Giglio, "A passive microwave technique for estimating rainfall and vertical structure information from space. Part I: Algorithm description," *J. Appl. Meteorol.*, vol. 33, no. 1, pp. 3–18, Jan. 1994.
[22] K. F. Evans, J. Turk, T. Wong, and G. L. Stephens, "A Bayesian approach to microwave precipitation profile retrieval," *J. Appl. Meteor.*, vol. 34, no. 1, pp. 260–279, Jan. 1995.

[23] C. Kummerow, W. S. Olson, and L. Giglio, "A simplified scheme for obtaining precipitation and vertical hydrometeor profiles from passive microwave sensors," *IEEE Trans. Geosci. Remote.*, vol. 34, no. 5, pp. 1213–1232, Sep. 1996.
[24] C. Kummerow *et al.*, "The evolution of the Goddard Profiling Algorithm (GPROF) for rainfall estimation from passive microwave sensors," *J. Appl. Meteorol.*, vol. 40, no. 11, pp. 1801–1820, Nov. 2001.
[25] C. D. Kummerow, S. Ringerud, J. Crook, D. Randel, and W. Berg, "An observationally generated a priori database for microwave rainfall retrievals," *J. Atmosp. Ocean. Technol.*, vol. 28, no. 2, pp. 113–130, Feb. 2011.
[26] R. W. Spencer, D. W. Martin, B. B. Hinton, and J. A. Weinman, "Satellite microwave radiances correlated with radar rain rates over land," *Nature*, vol. 304, pp. 141–143, Jul. 1983.
[27] N. C. Grody, "Classification of snow cover and precipitation using the special sensor microwave imager," *J. Geophys. Res.*, vol. 96, no. D4, pp. 7423–7435, Apr. 1991.
[28] R. R. Ferraro, N. C. Grody, and G. F. Marks, "Effects of surface conditions on rain identification using the DMSP-SSM/I," *Remote Sens. Rev.*, vol. 11, no. 1–4, pp. 195–209, 1994.
[29] R. R. Ferraro, E. A. Smith, W. Berg, and G. J. Huffman, "A screening methodology for passive microwave precipitation retrieval algorithms," *J. Atmosp. Sci.*, vol. 55, no. 9, pp. 1583–1600, May 1998.
[30] W. S. Olson, C. D. Kummerow, G. M. Heymsfield, and L. Giglio, "A method for combined passive-active microwave retrievals of cloud and precipitation profiles," *J. Appl. Meteorol.*, vol. 35, no. 10, pp. 1763–1789, Oct. 1996.
[31] Z. Haddad *et al.*, "The TRMM 'day-1' radar/radiometer combined rain-profiling algorithm," *J. Meteorol. Soc. Jpn.*, vol. 75, no. 4, pp. 799–809, 1997.
[32] F. Marzano *et al.*, "Bayesian estimation of precipitating cloud parameters from combined measurements of spaceborne microwave radiometer and radar," *IEEE Trans. Geosci. Remote Sens.*, vol. 37, no. 1, pp. 596–613, Jan. 1999.
[33] M. Grecu and E. N. Anagnostou, "Use of passive microwave observations in a radar rainfall-profiling algorithm," *J. Appl. Meteorol.*, vol. 41, no. 7, pp. 702–715, Jul. 2002.
[34] M. Grecu, W. S. Olson, and E. N. Anagnostou, "Retrieval of precipitation profiles from multiresolution, multifrequency active and passive microwave observations," *J. Appl. Meteorol.*, vol. 43, no. 4, pp. 562–575, Apr. 2004.
[35] M. Grecu and W. S. Olson, "Bayesian estimation of precipitation from satellite passive microwave observations using combined radar-radiometer retrievals," *J. Appl. Meteorol. Climatology*, vol. 45, no. 3, pp. 416–433, Mar. 2006.
[36] G. M. Skofronick-Jackson *et al.*, "Combined radiometer-radar microphysical profile estimations with emphasis on high-frequency brightness temperature observations," *J. Appl. Meteorol.*, vol. 42, no. 4, pp. 476–487, Apr. 2003.
[37] G. W. Petty and K. Li, "Improved passive microwave retrievals of rain rate over land and ocean. 2. validation and intercomparison," *J. Atmosp. Ocean. Technol.*, vol. 30, no. 11, pp. 2509–2526, Nov. 2013.
[38] J. R. McCollum and R. R. Ferraro, "Microwave rainfall estimation over coasts," *J. Atmos. Ocean. Technol.*, vol. 22, no. 5, pp. 497–512, May 2005.
[39] S. T. Roweis and L. K. Saul, "Nonlinear dimensionality reduction by locally linear embedding," *Science*, vol. 290, no. 5500, pp. 2323–2326, Dec. 2000.
[40] W. Berg, T. L'Ecuyer, and C. Kummerow, "Rainfall climate regimes: The relationship of regional TRMM rainfall biases to the environment," *J. Appl. Meteorol. Climatology*, vol. 45, no. 3, pp. 434–454, Mar. 2006.
[41] C. Kummerow, W. Barnes, T. Kozu, J. Shiue, and J. Simpson, "The Tropical Rainfall Measuring Mission (TRMM) sensor package," *J. Atmosp. Ocean. Technol.*, vol. 15, no. 3, pp. 809–817, Jun. 1998.
[42] T. Iguchi, T. Kozu, R. Meneghini, J. Awaka, and K. I. Okamoto, "Rain-profiling algorithm for the TRMM precipitation radar," *J. Appl. Meteorol.*, vol. 39, no. 12, pp. 2038–2052, Dec. 2000.
[43] T. Wilheit, "A model for the microwave emissivity of the ocean's surface as a function of wind speed," *IEEE Trans. Geosci. Electron.*, vol. 17, no. 4, pp. 244–249, Oct. 1979.
[44] T. S. Lécuyer and G. L. Stephens, "An uncertainty model for Bayesian Monte Carlo retrieval algorithms: Application to the TRMM observing system," *Quart. J. R. Meteorol. Soc.*, vol. 128, no. 583, pp. 1713–1737, Jul. 2002.
[45] M. A. Janssen, *Atmospheric Remote Sensing by Microwave Radiometry*, M. A. Janssen, Ed. New York, NY, USA: Wiley, 1993.
[46] A. M. Ebtehaj, E. Foufoula-Georgiou, and G. Lerman, "Sparse regularization for precipitation downscaling," *J. Geophys. Res.*, vol. 117, no. D8, pp. 1–12, Apr. 2012.
[47] E. Foufoula-Georgiou, A. M. Ebtehaj, S. Q. Zhang, and A. Y. Hou, "Downscaling satellite precipitation with emphasis on extremes: A variational ℓ_1-norm regularization in the derivative domain," *Surveys Geophys.*, vol. 35, no. 3, pp. 1–19, May 2014.
[48] D. Donoho, "De-noising by soft-thresholding," *IEEE Trans. Inf. Theory*, vol. 41, no. 3, pp. 613–627, May 1995.
[49] R. Tibshirani, "Regression shrinkage and selection via the lasso," *J. R. Statist. Soc. Ser. B Stat. Methodol.*, vol. 58, no. 1, pp. 267–288, 1996.
[50] S. S. Chen, D. L. Donoho, and M. A. Saunders, "Atomic decomposition by basis pursuit," *SIAM J. Sci. Comput.*, vol. 20, no. 1, pp. 33–61, 1998.
[51] M. Elad, *Sparse and Redundant Representations: From Theory to Applications in Signal and Image Processing*. New York, NY, USA: Springer-Verlag, 2010.
[52] A. Tikhonov, V. Arsenin, and F. John, *Solutions of Ill-Posed Problems*. Washington, DC, USA: Winston & Sons, 1977.
[53] P. Hansen, *Discrete Inverse Problems: Insight and Algorithms*. Philadelphia, PA, USA: SIAM, 2010, vol. 7.
[54] H. Zou and T. Hastie, "Regularization and variable selection via the elastic net," *J. R. Statist. Soc. Ser. B Statist. Methodol.*, vol. 67, no. 2, pp. 301–320, Apr. 2005.
[55] Q. Li, R. L. Bras, and D. Veneziano, "Passive microwave remote sensing of rainfall considering the effects of wind and nonprecipitating clouds," *J. Geophys. Res., Atmosp.*, vol. 101, no. D21, pp. 26503–26515, Nov. 1996.
[56] S. Seto, N. Takahashi, and T. Iguchi, "Rain/No-Rain classification methods for microwave radiometer observations over land using statistical information for brightness temperatures under No-Rain conditions," *J. Appl. Meteorol.*, vol. 44, no. 8, pp. 1243–1259, Aug. 2005.
[57] T. D. Ellis, T. L'Ecuyer, J. M. Haynes, and G. L. Stephens, "How often does it rain over the global oceans? The perspective from CloudSat," *Geophys. Res. Lett.*, vol. 36, no. 3, pp. L03815-1–L03815-5, Feb. 2009.
[58] W. Berg, T. L'Ecuyer, and J. M. Haynes, "The distribution of rainfall over oceans from spaceborne radars," *J. Appl. Meteorol. Climatol.*, vol. 49, no. 3, pp. 535–543, Mar. 2009.
[59] S. Boyd and L. Vandenberghe, *Convex Optimization*. New York, NY, USA: Cambridge Univ. Press, 2004.
[60] S. Mehrotra, "On the implementation of a primal- interior point method," *SIAM J. Optim.*, vol. 2, pp. 575–601, 1992.
[61] C. Schumacher and R. A. Houze, "Comparison of radar data from the TRMM satellite and Kwajalein oceanic validation site," *J. Appl. Meteorol.*, vol. 39, no. 12, pp. 2151–2164, Dec. 2000.
[62] A. Behrangi, M. Lebsock, S. Wong, and B. Lambrigtsen, "On the quantification of oceanic rainfall using spaceborne sensors," *J. Geophys. Res.*, vol. 117, no. D20, p. 20105, 2012.

Ardeshir M. Ebtehaj was born in Tehran, Iran, in 1976. He received the B.Sc. and M.Sc. degrees in civil engineering from the Iran University of Science and Technology, Tehran, Iran, in 1999 and 2001, respectively, and the M.Sc. degree in mathematics and the Ph.D. degree in civil engineering from the University of Minnesota, Minneapolis, MN, USA, in 2013.

He is currently a Postdoctoral Research Fellow with the School of Civil and Environmental Engineering, College of Engineering, Georgia Institute of Technology, Atlanta, GA, USA. His research interests include stochastic hydrometeorology, computational remote sensing and data analysis, statistical machine learning, sparse modeling and applications of continuous optimization in land–atmosphere interactions, and water resources research.

Dr. Ebtehaj is currently a member of the Precipitation Technical Committee of the Hydrology Section of the American Geophysical Union. He was the recipient of an Outstanding Student Paper Award from the American Geophysical Union in 2011 and a NASA Earth and Space Science Fellowship from 2012 to 2013.

Rafael L. Bras received the B.S. and S.M. degrees in civil engineering and the Sc.D. degree in hydrology from the Massachusetts Institute of Technology (MIT), Cambridge, MA, USA, in 1972, 1974, and 1975, respectively.

From 1976 to 2008, he was a Professor with the Department of Civil and Environmental Engineering, School of Engineering, MIT, where he was the Director of the Ralph M. Parsons Laboratory from 1983 to 1991, was the Head of the Department from 1992 to 2001, and where he held a joint appointment with the Department of Earth, Atmospheric, and Planetary Sciences, School of Science from 1990 to 2008. From 2008 to 2010, he was the Dean of The Henry Samueli School of Engineering, University of California Irvine, Irvine, CA, USA. He is currently the Provost and Executive Vice President for Academic Affairs with the Georgia Institute of Technology, Atlanta, GA, USA, where he holds the K. Harrison Brown Family Chair with the School of Civil and Environmental, College of Engineering and with the School of Engineering and Earth and Atmospheric Sciences, College of Sciences. His research activities include remote sensing, hydrometeorology, hydroclimatology, land–atmosphere interactions, rainfall–runoff modeling, and fluvial geomorphology.

Dr. Bras is a Fellow of the American Society of Civil Engineers, the American Association for the Advancement of Science, the American Meteorological Society, and the American Geophysical Union, and he is a member of the National Academy of Engineering. He was the recipient of the Horton Medal of the American Geophysical Union, among other honors.

Efi Foufoula-Georgiou received the Diploma degree in civil engineering from the National Technical University of Athens, Athens, Greece, in 1979 and the M.Sc. and Ph.D. degrees in environmental engineering from the University of Florida, Gainesville, FL, USA, in 1982 and 1985, respectively.

From 1999 to 2003, she was the Director of the Saint Anthony Falls Laboratory, College of Science and Engineering, University of Minnesota, Minneapolis, MN, USA, and from 2008 to 2013, she was the Director of the National Center for Earth-Surface Dynamics, College of Science and Engineering, University of Minnesota, which is a National Science Foundation Science and Technology Center. She is currently with the Department of Civil, Environmental, and Geo-Engineering, College of Science and Engineering, University of Minnesota, where she holds the position of Distinguished McKnight University Professor and the Joseph T. and Rose S. Ling Chair in Environmental Engineering. Her research interests include the stochastic modeling of surface hydrologic and geomorphologic processes, the remote sensing estimation of space–time rainfall, the stochastic theories of transport on the Earth's surface, river network dynamics, and channel morphology.

Dr. Foufoula-Georgiou is a Fellow of the American Geophysical Union and the American Meteorological Society, and she is a member of the European Academy of Sciences. She was a recipient of the John Dalton Medal of the European Geophysical Society and the American Geophysical Union Hydrologic Sciences Award.